Computers and Structures 254 (2021) 106614

Contents lists available at ScienceDirect

Computers and Structures

journal homepage: www.elsevier.com/locate/compstruc

Review

Classical molecular dynamics simulations of the deformation of metals under uniaxial monotonic loading: A review

A. Kedharnath *, Rajeev Kapoor, Apu Sarkar

Mechanical Metallurgy Division, Bhabha Atomic Research Center, Mumbai 400085, India
Division of Engineering Sciences, Homi Bhabha National Institute, Anushaktinagar, Mumbai 400094, India

ARTICLE INFO

Article history:
Received 18 January 2021
Accepted 8 June 2021

Keywords:
Classical molecular dynamics
Single crystal
Grain boundary
Voids and cracks
Uniaxial simulation

ABSTRACT

Nanoscale features present in structural and functional materials affect their macroscopic properties and hence have been extensively studied. As experimental investigations of different nanoscale events can be tedious, computational techniques evolved as a cost-cutting method to replace or complement difficult to perform experiments. Classical molecular dynamics (MD) simulation is an effective tool to study the effect of specific nanostructural features on the overall mechanical behavior of the material. This article reviews the MD simulation of the mechanical behavior of metal crystals under uniaxial monotonic loading with and without the presence of defects such as grain boundaries (GBs), voids, and cracks. MD simulations showed that along with shear stress obtained through the Schmid factor, the normal stress to the slip plane also influenced the slip of the single crystals, and that the stacking fault energy (SFE) controlled dislocation and twin nucleation. GBs were observed to be regions of dislocation nucleation. Along with the grain size effect, the SFE also affected the deformation mechanism, such as changing it from dislocation slip in the grain to GB slip. MD simulations showed that voids and cracks emit dislocations and that the type of dislocations emitted depended on the SFE of the material. The nucleation of trailing partial dislocations on an adjacent plane to the leading partials resulted in twin formation. For configurations containing both GB and cracks, MD simulations showed that twist GBs were more resistant to crack propagation as compared to tilt GBs. The critical stress required for dislocation nucleation from the GB was dependent on its GB energy and structure. In presence of low angle GBs and Σ GBs, voids became energetically favorable sites for dislocation nucleation. Low angle GBs and Σ GBs require higher critical stress for dislocation nucleation as compared to voids.

Contents

* Corresponding author.
E-mail address: kedharnath1992@gmail.com (A. Kedharnath).

https://doi.org/10.1016/j.compstruc.2021.106614
0045-7949/

1. Introduction

With an increase in computing facilities, computational research groups have emerged [1] across the globe in recent decades and joined hands with experimentalists to solve engineering problems in a short time and with limited funds [2]. Theoretical researchers have also joined computational research groups to model and predict the properties of materials [3,4]. Even a few researchers have considered computational simulation as a third branch in addition to experiments and theoretical works [3,4]. These groups also have come up with computational software, codes, and tools to study and simulate various properties of materials using mathematical models and techniques. Computational techniques are helping researchers to plan and execute necessary experiments judiciously, saving time, and resources [5,6]. Along with experiments, computational simulations help achieve a deeper understanding of basic science as well as develop an ability for the lifetime prediction of structural materials [7–9]. Further, computational simulations help in optimizing the parameters in complex problems and reduce the risk of performing experiments involving radiation or biological or toxic materials [2,6]. Computational simulations can perform and visualize events that are difficult or expensive through experimental procedures [10]. However, they are based on assumptions and approximations and hence could lead to errors when compared to experiments [4]. The ability of the computational tool to predict the correct output efficiently depends on both the method of minimization of errors (desired accuracy) and the algorithm for the fast convergence of the solution [2].

Although the bulk properties and behavior of materials can be different depending on the length scale, for example, that at nano and micron-scale [1,11,12], the features at the nanoscale fundamentally affect the bulk properties [8,13,14]. For example, a few atoms of dopant can change the type of semiconductor and its conductivity [14]. The study of materials at the nanoscale has opened a field called nanotechnology [8]. It has been 60 years since Richard Feynman's "*There's Plenty of Room at the Bottom...*" [15] talk but there is still a large scope to study materials at the nanoscale level. Nanotechnology has scaled down devices to make possible the use of smart devices in our daily lives [1,8]. Nanomaterials or materials at the nanoscale have many interesting features such as point defects, voids, dislocations, grain boundaries (GBs), precipitates, etc. [1] which are distinct from bulk features in their appearance and behavior and hence affect the properties compared to corresponding bulk materials [14]. Both nanoscale and bulk properties can be studied using various computational techniques developed to probe features at different time and length scales [1,11]. Atomistic simulation such as classical molecular dynamics (MD) is one such technique used to study nanoscale events [10,16] that are otherwise difficult to perform through experimental methods [4,17]. One example is the study of materials at the nanoscale using Transmission Electron Microscope (TEM) [1,18] and here MD can complement TEM with help in visualization of the evolution of events [19]. The events that happen or evolve dynamically at fractions of seconds are difficult to capture experimentally [6,20]. One such example of a type of study by MD simulation is the collision cascade in an irradiation environment which lasts for fractions of a nanosecond [21]. Nanoscale events such as the interaction of dislocations, nanoprecipitates, nanocracks, and GBs, which affect the mechanical behavior of the material, can be studied effectively using MD [1,22]. Further, the MD technique can also be used to visualize and validate the mathematical deformation models for metals. One of the advantages of MD simulation is that it can study specific nano-scale events [17], for example, the interaction of dislocation with a precipitate or GB [23], deformation of each crystal in a polycrystal, or deformation of single crystals [24]. Apart from the study of materials behavior, computational simulations can also calculate the basic properties of the materials [25].

The deformation behavior of the materials is affected by the mode of loading, temperature, strain rate, and microstructure, which in turn consists of different types and morphologies of dislocations, GBs [11], precipitates, cracks [26], and voids. The knowledge of the deformation behavior and mechanical properties at these conditions is important so as to be able to deploy the materials for specific applications [8]. The desired mechanical properties can be achieved by modifying features at the micro and nano scales. For example, the magnitude of the dislocation density or the areal fraction of special boundaries can change the mechanical properties [14]. Another example is the presence of radiation-induced point defects that can alter the strength and change the ductile to brittle transition temperature of materials [21,27,28]. This article reviews the use of MD simulations in bringing out the deformation behavior of metal crystals in the presence of voids/cracks and GBs/interfaces in FCC, BCC, and HCP metals.

2. Atomistic simulations

2.1. Multi-scale simulations

Multi-scale computational techniques aim at solving problems at different time and length scales [11]. The time scale ranges from femtoseconds to years and the length scale ranges from nanometers to meters. The basic building units in each time and length scale are distinct. For example, in the atomistic scale, atoms and dislocations are basic building units implemented through MD and dislocation dynamics (DD) techniques [29–31], respectively. In these simulations time and length scales are independent variables, whereas material properties such as elastic modulus, conductivity, strength, etc. are the depedent variables [13]. Mathematical models or a set of equations are formulated to correlate the independent and dependent variables [32]. Historically in some cases, mathematical models were formulated before experimental observations, for example, dislocations were modeled in the late 19th century while its observation using TEM was in the late 1950s [18]. So, it is important to correctly model the physical phenomena to mimic reality [33]. Necessary initial values and boundary conditions are applied to models to accurately arrive at the solution [13].

Fig. 1 illustrates the flow of computational techniques at different time and length scales. There is no single model or technique to

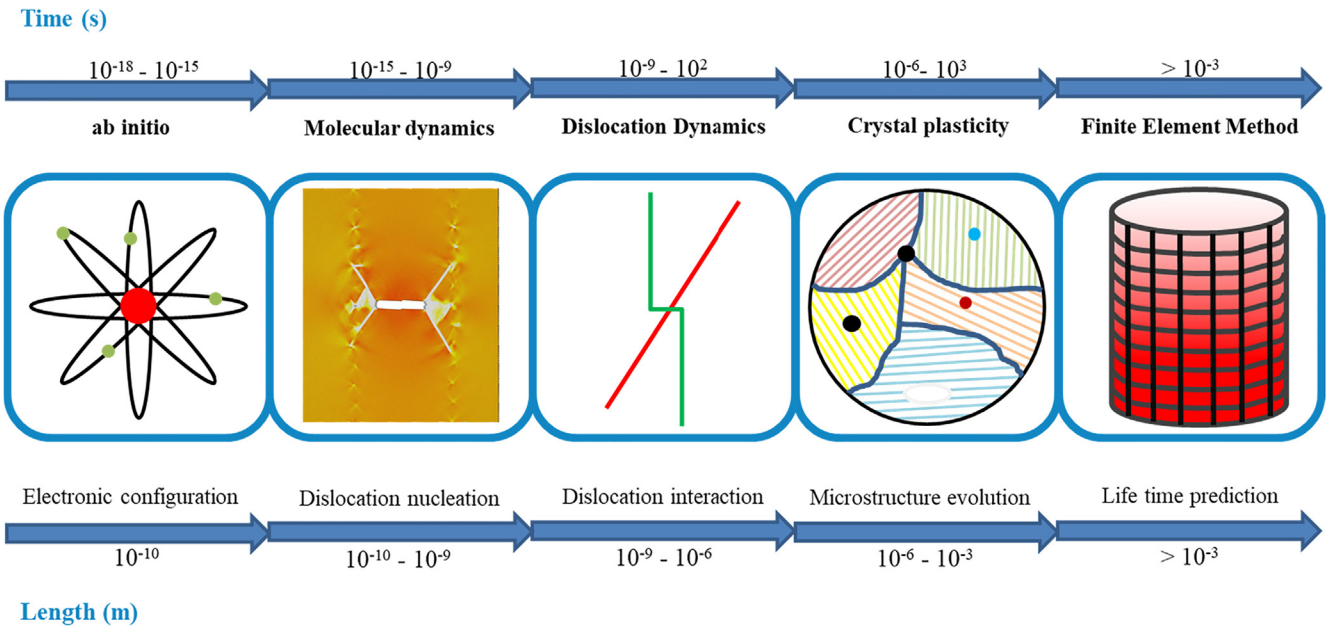

Fig. 1. Schematic showing multi-scale computational techniques and their time and length scales.

solve problems covering all time and length scales [34]. Each computational technique not only focuses on solving the problems within a particular scale but also passes the output to other scale techniques to create a multiscale picture of the problem [11]. Ab initio method involves a calculation of the electronic structure of the elements. While the ab initio method is useful in studying the basic properties of the materials, it fails to handle a larger number of atoms [1,25]. MD can handle a few millions of atoms. The input for MD comes from ab initio calculations/density functional theory (DFT) involving electronic configurations of the atoms [10]. MD can calculate the mobility of the dislocations both in the matrix and in the presence of obstacles (precipitate, interface). The output from MD is transferred to DD to calculate hardening parameters due to dislocation interaction with itself [11] and with the precipitates. Large strain problems and dislocation interaction with GBs increase the complexity with the standalone DD technique [11]. Crystal plasticity (CP) takes in the hardening parameters to study the microstructure and texture evolution. In general, the continuum method cannot deal with sharp interfaces like GBs making it difficult to study the evolution of nanoscale features [14]. It is also difficult to incorporate the orientation details into the continuum model [35]. However, it is to be noted that there are MD/Finite element approaches with assumptions and limitations to study nanoscale features [10,36]. Budarapu et al. [37] and Talebi et al. [38] formulated a coarse-grained technique to study fracture through multiscale methods from atomistic to coarse-grained and presented an open-source software PERMIX [38]. The Finite Element Method (FEM) uses the stress–strain relation from CP to explore real-life problems on structural components. The "bottom-up approach" in Fig. 1 is related to the deformation problem. A similar flow of computational techniques is available for various other problems [1,13,33]. This article focusses on the MD technique to study the deformation behavior at the nanoscale level and possible outputs that can be transferred to the higher scales. The most common MD code used by many researchers from various fields is LAMMPS (Large-scale Atomic/Molecular Massively Parallel Simulator)[39]. Other common MD codes/software are GROMACS [40], NAMD [41] and CHARMM [42].

2.2. Classical molecular dynamics technique

MD is essentially the application of classical mechanics to treat the evolution of atoms interacting via a determined potential at nanometer length and picosecond time scales. It is now almost 70 years since the first paper describing the use of MD was published. In the year 1952, Green used autocorrelation functions to study transport coefficients [43]. Using his formulations, researchers started working on conductivity problems [44]. Since conductivity simulations didn't give the desired results, researchers moved to viscosity problems [45]. Ashurst and Hoover successfully simulated steady flow by maintaining the temperature using a reservoir [5,45]. With the improvement in the boundary conditions in a system with a reservoir, dynamic simulations of radiation damage [46] and shockwave were successful [47]. After these successful simulations, modifications in algorithms, ensembles, and interatomic potentials improved the MD technique. Verlet came up with an easy algorithm to integrate Newton's equation on a thousand-particles system [48]. Nose extended the usage of the ensemble in MD simulations by independently maintaining the pressure [49] and temperature [50] constant. Holian and Ravelo modified the interatomic potential to study brittle fracture using non-equilibrium molecular dynamics (NEMD) [51]. Kröger et al. modified NEMD to analyze the plastic yield of metal [9]. In 1976, Ashurst and Hoover studied fracture of crystals using Newton's equations of motion [5]. In 1981, Parrinello and Rahman studied the deformation of nickel by applying uniaxial stress using MD [22]. Following them, there were a lot of research works on the deformation of metals using MD in the late 20th century [12,45,51–55]. Now, MD has emerged as an indispensable technique in the field of physics, chemistry, biology, and materials science [3].

MD is a powerful computational technique to study the dynamics of many-body systems [3]. MD is successful in studying nanoscale features as fundamentally all the material's properties came out as a consequence of the arrangement and interaction of atoms [18]. The quotes by Democritus' "*...in reality there are atoms and the void...*" [33] and Richard Feynman "*...I, a universe of atoms, an atom in the universe*" emphasize the importance of atoms. With

the initial input of position and velocity of atoms, MD uses Newton's law of motion to calculate the trajectories of atoms [2].

$$\boldsymbol{F} = m\boldsymbol{a} = m\frac{d\boldsymbol{v}}{dt} = m\frac{d^2\boldsymbol{r}}{dt^2} \tag{1}$$

$$\boldsymbol{v}(t) = \frac{\boldsymbol{x}(t+\Delta t) - \boldsymbol{x}(t-\Delta t)}{2\Delta t} \tag{2}$$

$$\boldsymbol{x}(t+\Delta t) = 2\boldsymbol{x}(t) - \boldsymbol{x}(t-\Delta t) + \boldsymbol{a}(t)\Delta t^2 \tag{3}$$

Integrating Newton's equation (1) gives position and velocity as a function of time. Equation (3) gives the position of atoms at $t+\Delta t$ when the position and velocity of atoms at t are known. The time-step Δt is chosen as a small value in picoseconds so as to reduce the error between the previous and current atomic positions during the integration process [2]. The interaction of atoms is given by interatomic potentials which describe the accuracy of the MD simulations [1]. During initial deformation studies using MD, Lennard-Jones (LJ) and Morse potentials were used [51,56,57]. The pair potential energy (E_{ij}^{LJ}) between two atoms i and j described by LJ potential [58] is given by

$$E_{ij}^{LJ} = 4\varepsilon_{ij}\left[\left(\frac{\sigma_{ij}}{r_{ij}}\right)^{12} - \left(\frac{\sigma_{ij}}{r_{ij}}\right)^{6}\right] \tag{4}$$

ε_{ij} is the depth of the potential well, σ_{ij} is the equilibrium distance, and r_{ij} is the distance between the atoms. The LJ potential is used for faster and cost-effective simulations but does not accurately predict metallic properties such as elastic contacts and stacking fault energy (SFE) [59]. Morse potential is another simple two-body potential used to study systems involving non-metallic and metallic elements such as C-Al [58]. The Morse pair potential energy (E_{ij}^{Morse}) is defined by - D_0 is the depth of the potential well, α is the elastic modulus, r_{ij} is the distance between the atoms, and r_0 is the equilibrium distance.

$$E_{ij}^{Morse} = D_0\left[e^{-2\alpha\left(r_{ij}-r_0\right)} - 2e^{-\alpha\left(r_{ij}-r_0\right)}\right] \tag{5}$$

During simulations of tensile deformation of metals by Macmillan and Kelly [60], the system became unstable while using the Morse potential. The Morse potential could not predict the ideal strength of BCC metals [61]. Many-body potentials such as the Finnis-Sinclair (F-S) [62] and the embedded atom method (EAM) [63] potentials that emerged in the same year could predict metallic properties better than two-body potentials. The F-S potential consists of two parts – repulsive term $U(r_{ij})$ between atoms i and j separated by a distance of r_{ij} and cohesive term $\eta(r_{ij})$ based on second-moment approximation in tight-binding theory.

$$E_i^{F-S} = \frac{1}{2}\sum_{j\neq i} U(r_{ij}) - \sqrt{\sum_{j\neq i}\eta(r_{ij})} \tag{6}$$

The EAM potential [9,51] is widely used for metallic elements (say α and β), as it can explain both the electronic part $U_\alpha \& \rho(\boldsymbol{r})$ and pairwise part $\phi(\boldsymbol{r})$ of the interaction of the atoms i to j. The computational cost is twice while using the EAM potential than the LJ potential. However, the EAM potential can accurately predict lattice parameters, elastic constants, and SFE of the metals. The EAM potential is expressed as

$$E_i^{EAM} = U_\alpha\left(\sum_{j\neq i}\rho_\beta(\boldsymbol{r}_{ij})\right) + \frac{1}{2}\sum_{j\neq i}\phi_{\alpha\beta}(\boldsymbol{r}_{ij}) \tag{7}$$

where $\boldsymbol{r_{ij}}$ is the separation distance between atoms i to j, U_α is the energy required to embed an atom in the electron cloud, and $\rho(\boldsymbol{r})$ is the electron transfer function between the atoms [2]. Various EAM potentials were developed and modified to study mechanical properties; further details on this can be found in reference [64–66]. The Force ($\boldsymbol{F}$) and the interatomic potential (E) are connected by the equation $\boldsymbol{F} = -\nabla E$ where E can be either E_{ij}^{LJ} or E_{ij}^{Morse} or E_i^{F-S} or E_i^{EAM}. The potentials discussed above have been modified and used for various computational studies, however, here, the potentials are grouped under either LJ, Morse, F-S or EAM in the Tables 1, 2, and 3.

Equations (1)–(3) compute the changes in position and velocity and thereby change the force and energy of the system. To compute the macroscopic properties of materials, ensembles are used. The system can be in either of the below ensembles depending on the following [2]:

1) Microcanonical ensemble (NVE): constant number of atoms, volume, and energy.
2) Isothermal–isobaric ensemble (NPT): constant number of atoms, pressure, and temperature.
3) Canonical ensemble (NVT): constant number of atoms, volume, and temperature.
4) Grand canonical ensemble (μVT): constant chemical potential, volume, and temperature.
5) Isoenthalpic–isobaric ensemble (NPH): constant number of atoms, pressure, and enthalpy.

The material properties change dynamically in a MD simulation during transient and steady states. The averaged value of a material property can be calculated either by averaging the values taken from various simulations or by averaging the values taken at various time steps in a single simulation. The earlier method is termed as ensemble average and the latter method is termed as time average. According to the ergodic hypothesis, the ensemble average is equivalent to the time average, and thus the properties in a single simulation can be used to determine the average values [2]. Thermodynamic properties such as temperature T and pressure P are be calculated using the following equations [67]:

$$T = \frac{2}{3Nk}\sum_i^N \frac{m_i\boldsymbol{v_i^2}}{2} \tag{8}$$

$$P_{ij} = \frac{\sum_a^N m_a \boldsymbol{v_{ai}}\boldsymbol{v_{aj}}}{V} + \frac{\sum_a^N \boldsymbol{r_{ai}}.\boldsymbol{F_{aj}}}{V} \tag{9}$$

where k is the Boltzmann constant, N is the number of atoms, T is the temperature, V is the volume of the system, m_a is the mass, $\boldsymbol{v_a}$ is the velocity, $\boldsymbol{r_a}$ is the position vector and $\boldsymbol{F_a}$ is the force vector of the atom a.

3. Deformation behavior of metals

The strength of a material depends on the length scale of its microstructural features. For a single-phase metal, it would depend on its dislocation spacing and grain size. Fig. 2 shows the variation of strength from a single crystal to ultra-fine grain metals. The red-colored regions represent single crystal and nanocrystal configurations. The red-colored region also represent single crystal configurations in the presence of defects such as voids, dislocations, cracks, and GBs. The blue-colored region represents structural materials ranging from polycrystal to ultra-fine grain metals. The experimental tensile strength values presented in Fig. 2b have been taken from these articles [68–74]. For a single crystal, defect types and their configurations play a role in its strength. The strength of a single crystal with no defects is the highest and with an increase in the number of point defects the strength decreases drastically. With the presence of dislocations and interfaces, the

Table 1
The maximum stress of single crystal configurations during uniaxial simulations. The interatomic potentials used in the simulations are shown with their corresponding references. F-S refer to the Finnis-Sinclair potential and EAM refer to the embedded atom method potential. For data not available in the literature, the corresponding cells are left blank.

Literature and axis of pulling	Metal	Crystal structure	Atomic number (Z)	Temperature (K)	Strain rate (/ps)	Maximum stress (GPa)	Interatomic potential
Lynden-Bell(1995) [53] [100]	Pt	FCC	78	0		26.00	F-S (Sutton 1990[109])
	Rh	FCC	45	0		28.70	
	Au	FCC	79	0		14.82	
	Ag	FCC	47	0		11.77	
Branício(2000)[57] ⟨001⟩	Ni	FCC	28	300	5×10^{-4}	8.87	EAM (Chantasiriwan 1998[110])
	Ni	FCC	28	300	5×10^{-3}	9.25	
	Ni	FCC	28	300	5×10^{-2}	11.85	
	Ni	FCC	28	300	7×10^{-2}	12.78	
	Ni	FCC	28	300	0.15	15.92	
Komanduri(2001) [80] [001]	Al	FCC	13	293		6.45	Morse (Morse 1929[111])
	Cu	FCC	29	293		14.27	
	Ni	FCC	28	293		17.96	
	Fe	BCC	26	293		14.32	
	Cr	BCC	24	293		15.52	
	W	BCC	74	293		25.59	
Koh(2005)[79] [001]	Pt	FCC	78	50	4×10^{-4}	12.19	F-S (Sutton 1990[109])
	Pt	FCC	78	300	4×10^{-4}	8.47	
	Pt	FCC	78	50	4×10^{-3}	13.18	
	Pt	FCC	78	300	4×10^{-3}	9.33	
	Pt	FCC	78	50	4×10^{-2}	18.35	
	Pt	FCC	78	300	4×10^{-2}	11.98	
Chen(2005)[90] [001]	Au	FCC	79	200	0.2	10.81	EAM (Johnson 1988[112])
	Au	FCC	79	300	0.2	10.18	
	Au	FCC	79	400	0.2	9.40	
	Au	FCC	79	500	0.2	8.46	
	Au	FCC	79	600	0.2	8.21	
Rabkin(2007)[75] [001]	Au	FCC	79	0	1×10^{-4}	2.67	EAM (Foiles 1986[113], Cai 1996[114], Grochola 2005[115])
	Au	FCC	79	50	1×10^{-4}	2.21	
	Au	FCC	79	100	1×10^{-4}	1.91	
	Au	FCC	79	150	1×10^{-4}	1.68	
	Au	FCC	79	200	1×10^{-4}	1.50	
	Au	FCC	79	300	1×10^{-4}	1.09	
	Au	FCC	79	500	1×10^{-4}	0.74	
Wang(2007)[82] [100]	Cu	FCC	29	293	1.3×10^{-2}	0.60	EAM (Johnson 1988[112])
	Cu	FCC	29	293	1.3×10^{-3}	0.46	
	Cu	FCC	29	293	1.6×10^{-4}	0.38	
Setoodeh(2008)[61] [100]	Ni	FCC	28	100		10.76	EAM (Oh 1988 [116])
	Ni	FCC	28	200		9.61	
	Ni	FCC	28	300		8.51	
	Ni	FCC	28	400		7.71	
	Ni	FCC	28	500		6.50	
Wen(2008)[89] [001]	Ni	FCC	28	300	1×10^{-4}	7.99	F-S (Sutton 1990[109])
	Ni	FCC	28	300	1×10^{-3}	8.15	
	Ni	FCC	28	300	2×10^{-3}	8.32	
	Ni	FCC	28	300	5×10^{-3}	8.49	
	Ni	FCC	28	300	1×10^{-2}	8.88	
	Ni	FCC	28	300	2×10^{-2}	9.30	
	Ni	FCC	28	300	5×10^{-2}	9.95	
	Ni	FCC	28	300	8×10^{-2}	10.27	
	Ni	FCC	28	300	0.1	10.85	
	Ni	FCC	28	300	0.14	11.33	
Lao(2013)[6] ⟨100⟩	Au	FCC	79	2		4.2	EAM (Daw 1984 [63])
	Cu	FCC	29	300		4.9	
	Ni	FCC	28	300		8.3	
	Pd	FCC	46	100		7.5	
Xu(2013)[99] [001]	Al	FCC	13	10	6×10^{-4}	2.22	EAM (Voter 1987 [117])
	Al	FCC	13	300	6×10^{-4}	1.11	

(continued on next page)

Table 1 (*continued*)

Literature and axis of pulling	Metal	Crystal structure	Atomic number (Z)	Temperature (K)	Strain rate (/ps)	Maximum stress (GPa)	Interatomic potential
Wang(2013)[100] ⟨100⟩	Ni	FCC	28	0	1.4×10^{-3}	14.80	EAM (Daw 1984 [63])
	Ni	FCC	28	300	1.4×10^{-3}	11.10	
	Ni	FCC	28	600	1.4×10^{-3}	8.60	
	Ni	FCC	28	900	1.4×10^{-3}	6.50	
	Ni	FCC	28	1200	1.4×10^{-3}	4.20	
	Ni	FCC	28	1500	1.4×10^{-3}	2.00	
	Ni	FCC	28	0	5.5×10^{-3}	5.80	
	Ni	FCC	28	300	5.5×10^{-3}	12.00	
	Ni	FCC	28	600	5.5×10^{-3}	9.20	
	Ni	FCC	28	900	5.5×10^{-3}	6.90	
	Ni	FCC	28	1200	5.5×10^{-3}	4.70	
	Ni	FCC	28	1500	5.5×10^{-3}	2.50	
	Ni	FCC	28	0	9.7×10^{-3}	3.50	
	Ni	FCC	28	300	9.7×10^{-3}	12.20	
	Ni	FCC	28	600	9.7×10^{-3}	9.50	
	Ni	FCC	28	900	9.7×10^{-3}	7.10	
	Ni	FCC	28	1200	9.7×10^{-3}	4.90	
	Ni	FCC	28	1500	9.7×10^{-3}	2.70	
	Ni	FCC	28	0	1.4×10^{-2}	2.50	
	Ni	FCC	28	300	1.4×10^{-2}	11.50	
	Ni	FCC	28	600	1.4×10^{-2}	9.60	
	Ni	FCC	28	900	1.4×10^{-2}	7.40	
	Ni	FCC	28	1200	1.4×10^{-2}	5.00	
	Ni	FCC	28	1500	1.4×10^{-2}	2.60	
Amigo(2014)[101] [100]	Cu	FCC	29	0.1	1×10^{-4}	11.70	EAM (Williams 2006 [118])
	Cu-0.1at. % Ag	FCC	29	0.1	1×10^{-4}	11.50	
	Cu-0.2at. % Ag	FCC	29	0.1	1×10^{-4}	11.10	
	Cu-0.3at. % Ag	FCC	29	0.1	1×10^{-4}	11.00	
	Cu-0.4at. % Ag	FCC	29	0.1	1×10^{-4}	10.90	
	Cu-0.5at. % Ag	FCC	29	0.1	1×10^{-4}	10.70	
	Cu	FCC	29	100	1×10^{-4}	10.19	
	Cu-0.2at. % Ag	FCC	29	100	1×10^{-4}	9.69	
	Cu-0.4at. % Ag	FCC	29	100	1×10^{-4}	9.69	
	Cu	FCC	29	300	1×10^{-4}	7.39	
	Cu-0.2at. % Ag	FCC	29	300	1×10^{-4}	6.50	
	Cu-0.4at. % Ag	FCC	29	300	1×10^{-4}	7.03	
Ren(2014)[102] [0001]	Ti	HCP	22	300	1×10^{-4}	4.63	EAM (Zope 2003 [119], Kim 2006[120]) and F-S (Ackland 1992 [121])
Aghababaei(2014) [103] ⟨0001⟩	Mg	HCP	12	5	1×10^{-3}	8.90	EAM (Sun 2006 [122])
Healy(2014)[104] [001]	Fe	BCC	26	300	2.5×10^{-4}	1.92	EAM (Mendelev 2003 [123])
Saha(2016)[105] ⟨100⟩	W	BCC	74	10	1×10^{-3}	23.72	EAM (Daw 1984 [63])
	W	BCC	74	100	1×10^{-3}	18.13	
	W	BCC	74	500	1×10^{-3}	13.23	
	W	BCC	74	1000	1×10^{-3}	12.78	
	W	BCC	74	1500	1×10^{-3}	9.65	
Ma(2016)[98] [100]	W	BCC	74	293		16.50	EAM (Zhou 2004 [124])
	W	BCC	74	473		15.40	
	W	BCC	74	673		12.00	
	W	BCC	74	873		10.60	
	W	BCC	74	1073		9.90	
Mahata(2016)[59]	Mg-5Li	HCP	12	4.2	1×10^{-5}	0.49	EAM (Kim 2012 [125])
	Mg-5Li	HCP	12	4.2	1×10^{-4}	0.49	
	Mg-5Li	HCP	12	4.2	1×10^{-3}	0.53	
	Mg-5Li	HCP	12	4.2	1×10^{-2}	0.55	
	Mg-5Li	HCP	12	300	1×10^{-3}	0.48	
	Mg-5Li	HCP	12	500	1×10^{-3}	0.36	

Table 1 (*continued*)

Literature and axis of pulling	Metal	Crystal structure	Atomic number (Z)	Temperature (K)	Strain rate (/ps)	Maximum stress (GPa)	Interatomic potential
An(2017)[106] [0001]	Ti	HCP	22	10	6×10^{-4}	10.21	EAM (Zhou 2001 [126])
	Ti	HCP	22	300	6×10^{-4}	8.33	
Chang(2017)[107] Chang(2018) [108] [0001]	Ti	HCP	22	300	1×10^{-4}	4.47	F-S (Ackland 1992 [121])
	Ti	HCP	22	300	1×10^{-3}	5.22	
	Ti	HCP	22	300	2×10^{-3}	5.39	
	Ti	HCP	22	300	5×10^{-3}	5.72	
	Ti	HCP	22	300	8×10^{-3}	6.30	
	Ti	HCP	22	300	1×10^{-2}	6.27	
	Ti	HCP	22	300	2×10^{-2}	7.47	
	Ti	HCP	22	300	5×10^{-2}	9.11	
	Ti	HCP	22	300	8×10^{-2}	9.69	
	Ti	HCP	22	300	0.1	10.30	

Table 2
The maximum stress of GB/interface configurations during uniaxial simulations. The interatomic potentials used in the simulations are shown with their corresponding refered literature. The cell(s) in Table 2 are left blank as there is no value found in the literature.

Literature and loading direction to the GB plane	Metal	GB type and their spacing (nm)	Atomic number (Z)	Temperature (K)	Strain rate (/ps)	Maximum stress (GPa)	Interatomic potential
Afanasyev(2007)[141] Perpendicular	Au	Twin – 0	79	300	3×10^{-5}	4.60	EAM (Foiles 1986 [113])
	Au	18.2	79	300	3×10^{-5}	4.60	
	Au	12.2	79	300	3×10^{-5}	4.61	
	Au	7.3	79	300	3×10^{-5}	4.88	
	Au	4.1	79	300	3×10^{-5}	4.91	
	Au	2.1	79	300	3×10^{-5}	5.35	
Liu(2016)[88] Random	Ni	Twin – 1.22	28	300	1×10^{-3}	3.47	EAM (Mishin 1999 [150])
	Ni	2.44	28	300	1×10^{-3}	3.70	
	Ni	3.66	28	300	1×10^{-3}	3.93	
	Ni	4.88	28	300	1×10^{-3}	3.77	
	Ni	6.10	28	300	1×10^{-3}	3.66	
	Ni	7.32	28	300	1×10^{-3}	3.50	
Borovikov(2017)[148] Perpendicular	Cu	Σ11 – 17	29	300	1×10^{-4}	2.50	EAM (Williams 2006 [118])
	Ag	17	47	300	1×10^{-4}	1.68	
Zhao(2018)[149] Perpendicular	Fe	Twin – 1.98	26	300	5×10^{-4}	12.14	EAM (Mendelev 2003 [123])
	Fe	7.92	26	300	5×10^{-4}	12.97	
Parallel	Fe	1.98	26	300	5×10^{-4}	24.60	
	Fe	7.92	26	300	5×10^{-4}	25.11	

strength reduces further from GPa to MPa. Depending on the processing methods, the strength may vary in the range of a few 100 MPa. Severe plastic deformation gives rise to ultra-fine grains in the metals resulting in higher strength than that of fine-grain polycrystals, due to the Hall-Petch strengthening effect [1,72]. Nanograins/particles exhibit higher strength due to the confinement of dislocation within a small particle or grain [75].

This article focusses on nano-length scale features evolving at a nano-time scale period whose strength lies in the range of a few GPa as seen in the red-colored region in Fig. 2. Nano-length scale features in a metallic system include point defects, dislocation, GBs, and nano-time scale events include dislocation motion and their interaction, nanocrack blunting and growth which forms the basis for deformation mechanism at the nanoscale [11]. The testing method of the nanoscale features and observation of the nanoscale events using the atomistic simulations are similar to experiments that are discussed in the sections below. The strain rate in MD simulations is relatively high compared to that in experiments, primarily due to the small timestep required during the simulation. This is also a reason for the high value of the strength of the material obtained in the MD simulations. Not being able to achieve realistic strain rates is a limitation of MD. However, despite the high strain rates, MD simulations could still be used to determine basic strain rate-independent material properties and to study the general mechanical behavior of nanomaterials [76]. The stress response of the system can be calculated in two ways: (i) the total pressure of the system from equation (9), and (ii) the stress per-atom, which helps in visualizing the stress gradient at dislocation core, crack tip, and GB/interface. The stress tensor (σ_{ij}) for an atom consist of two terms – kinetic energy term (mv_iv_j) and virial term. The virial term consists of pairwise energy contribution (for N_p atoms), bond contribution (for N_b atoms), angle (for N_a atoms), dihedral (for N_d atoms), improper (for N_i atoms) and long-range Coulombic interactions (Kspace) and internal constraint forces (for N_f atoms) [77–79].

Table 3
The maximum stress of single crystal configurations in the presence of void/crack during uniaxial simulations. The characteristics of the void and crack configurations are given in the first column of the table. The interatomic potentials used in the simulations are shown with their corresponding references. F-S refer to the Finnis-Sinclair potential and EAM refer to the embedded atom method. Some cells in table 3 are left blank as for those conditions no values were found in the literature.

Literature, axis of pulling, and characteristics of void/crack	Metal	Void diameter/crack length (nm)	Atomic number (Z)	Temperature (K)	Strain rate (/ps)	Maximum stress (GPa)	Interatomic potential
Potirniche(2006)[163] [100], center cylindrical-void	Ni	1.52	28	300	1×10^{-2}	12.02	EAM (Daw 1984 [63])
	Ni	3.06	28	300	1×10^{-2}	9.68	
	Ni	6.08	28	300	1×10^{-2}	9.12	
	Ni	9.04	28	300	1×10^{-2}	8.18	
Traiviratana(2008)[164] [001], center spherical-void	Cu	1.00	29		1×10^{-4}	11.24	EAM (Mishin 2001 [169])
		2.00	29		1×10^{-4}	8.75	
		4.00	29		1×10^{-4}	6.94	
		8.00	29		1×10^{-4}	5.62	
Tang(2012)[159] [001], center spherical-void	Cu	0.78	29	300	1×10^{-3}	2.46	F-S (Dai 2006 [111])
	Cu	1.16	29	300	1×10^{-3}	2.41	
	Cu	1.96	29	300	1×10^{-3}	2.12	
	Cu	3.84	29	300	1×10^{-3}	1.66	
	Cu	7.76	29	300	1×10^{-3}	1.29	
	Cu	11.56	29	300	1×10^{-3}	1.08	
	Cu	15.44	29	300	1×10^{-3}	0.97	
	Ta	1.00	73	300	1×10^{-4}	3.48	
	Ta	2.00	73	300	1×10^{-4}	2.90	
	Ta	3.00	73	300	1×10^{-4}	2.64	
	Ta	4.00	73	300	1×10^{-4}	2.55	
	Ta	5.00	73	300	1×10^{-4}	2.32	
	Ta	6.64	73	300	1×10^{-4}	2.13	
	Ta	10.00	73	300	1×10^{-4}	1.95	
	Ta	14.94	73	300	1×10^{-4}	1.81	
	Ta	22.04	73	300	1×10^{-4}	1.70	
	Ta	29.92	73	300	1×10^{-4}	1.59	
	Ta	44.92	73	300	1×10^{-4}	1.64	
	Ta	59.94	73	300	1×10^{-4}	1.53	
	Ta	0.20	73	300	1×10^{-3}	3.52	
	Ta	0.40	73	300	1×10^{-3}	3.54	
	Ta	0.60	73	300	1×10^{-3}	3.64	
	Ta	1.00	73	300	1×10^{-3}	3.37	
	Ta	1.20	73	300	1×10^{-3}	3.32	
	Ta	1.40	73	300	1×10^{-3}	3.23	
	Ta	1.60	73	300	1×10^{-3}	3.02	
	Ta	2.00	73	300	1×10^{-3}	2.93	
	Ta	2.40	73	300	1×10^{-3}	2.78	
	Ta	3.00	73	300	1×10^{-3}	2.75	
	Ta	3.40	73	300	1×10^{-3}	2.61	
	Ta	4.00	73	300	1×10^{-3}	2.61	
	Ta	5.00	73	300	1×10^{-3}	2.49	
	Ta	6.00	73	300	1×10^{-3}	2.29	
	Ta	6.58	73	300	1×10^{-3}	2.14	
	Ta	7.90	73	300	1×10^{-3}	2.14	
	Ta	9.96	73	300	1×10^{-3}	2.01	
	Ta	22.04	73	300	1×10^{-3}	1.71	
Wen-Ping(2012)[161] [010], edge rectangular thru-thickness-crack; width 0.35 nm	Ni	3.52	28	0	2×10^{-4}	12.96	EAM (Mishin 1999 [150])
	Ni	3.52	28	30	2×10^{-4}	12.28	
	Ni	3.52	28	300	2×10^{-4}	13.32	
Zhang(2013)[35] [010], center rectangular thru-thickness-crack	Ni	10	28	0.1	2×10^{-5}	7.01	EAM (Angelo 1995 [170])
Cui(2014)[160100], edge rectangular thru-thickness-crack	Cu	1.15	29	0		7.63	EAM (Mishin 1999 [150])
	Cu	2.17	29	0		6.05	
	Cu	3.20	29	0		5.32	
	Cu	4.22	29	0		4.81	
	Cu	5.24	29	0		4.45	
	Al	1.29	13	0		5.95	
	Al	2.43	13	0		4.81	
	Al	3.58	13	0		4.64	
	Al	4.73	13	0		4.55	
	Al	5.87	13	0		4.36	
Aghababaei(2014)[103] ⟨0001⟩	Mg	0	12	5	1×10^{-3}	8.90	EAM (Sun 2006 [122])
Center spherical-void	Mg	2	12	5	1×10^{-3}	5.75	
Center square-crack	Mg	2	12	5	1×10^{-3}	5.09	

Table 3 (*continued*)

Literature, axis of pulling, and characteristics of void/crack	Metal	Void diameter/crack length (nm)	Atomic number (Z)	Temperature (K)	Strain rate (/ps)	Maximum stress (GPa)	Interatomic potential
Pei(2015)[165] Twin boundaries ahead of edge thru-thickness-crack	Ni	6.5	28	1.1	1×10^{-4}	6.07	EAM (Williams 2006 [118], Mendelev 2008 [171])
	Cu	6.5	29	1.1	1×10^{-4}	4.23	
	Ag	6.5	47	1.1	1×10^{-4}	2.69	
	Al	6.5	13	1.1	1×10^{-4}	1.93	
	Pd	6.5	46	1.1	1×10^{-4}	5.97	
	Pt	6.5	78	1.1	1×10^{-4}	5.79	
	Au	6.5	79	1.1	1×10^{-4}	4.38	
	Pb	6.5	82	1.1	1×10^{-4}	1.19	
Pei(2015)[166] Twin boundaries ahead of edge thru-thickness-crack	Cu	6.5	29	0.5	1×10^{-4}	4.51	EAM (Mishin 2001 [169])
	Cu	6.5	29	1.1	1×10^{-4}	4.51	
	Cu	6.5	29	2	1×10^{-4}	4.51	
	Cu	6.5	29	10	1×10^{-4}	4.51	
	Cu	6.5	29	30	1×10^{-4}	4.51	
	Cu	6.5	29	40	1×10^{-4}	7.25	
	Cu	6.5	29	60	1×10^{-4}	7.96	
Li(2015)[162] [010], center spherical-void	Ni	3.52	28	0	2×10^{-4}	14.92	EAM (Mishin 1999 [150])
Center rectangular thru-thickness-crack; width 0.7 nm	Ni	3.52	28	0	2×10^{-4}	13.49	
Chandra(2016)[167] [010], edge rectangular thru-thickness-crack; width 1.5 nm	Al	5.5	13	1	1×10^{-4}	4.30	EAM (Mishin 1999 [150])
Fang(2016)[168] [001], edge rectangular thru-thickness-crack	Al	6.08	13	50	1×10^{-3}	1.52	EAM (Mendelev 2008 [171])
Wang(2017)[87100], center cylindrical-void	Ni	10.56	28	300	5×10^{-4}	7.17	EAM (Mishin 1999 [150])

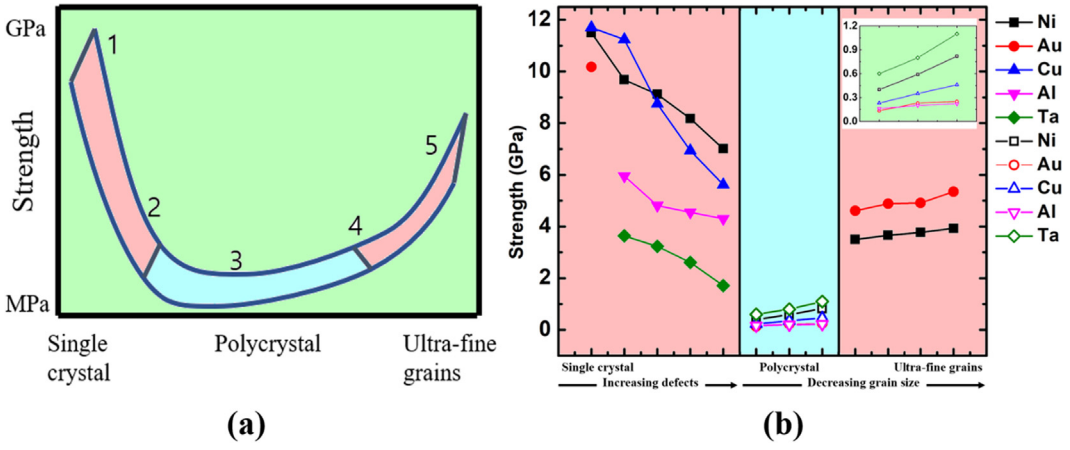

Fig. 2. (a) Schematic showing the strength of the metals ranging from single crystal to ultra-fine grain metals. The numbers along the curve represent the following. 1 - Single crystal, 2 – Single crystal with defects, 3 – Polycrystal, 4 – Processed metals, and 5 – Severely deformed metals. (b) Data points of strength of various metals collected from the literature are presented. The filled shapes represent data points from MD simulation results (is discussed in this article) and unfilled shapes represent data points from experimental results. The experimental tensile strength values are taken from the articles [68–74]. The red-colored regions represent single crystal configurations with various defects and nanocrystalline configurations studied using atomistic techniques (is discussed in this article). The blue-colored region represents structural materials. The subplot in Fig. 2b is a zoomed area of the polycrystal region. (For interpretation of the references to color in this figure legend, the reader is referred to the web version of this article.)

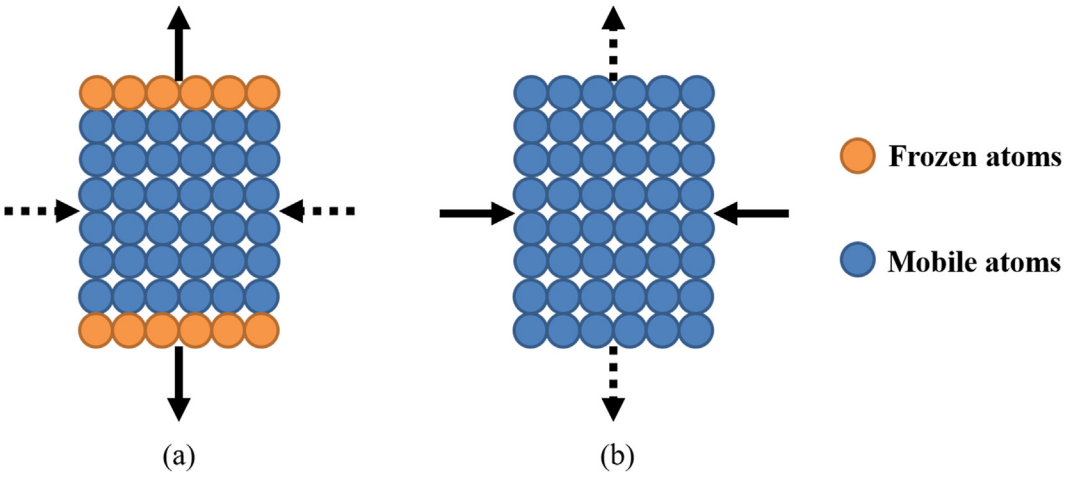

Fig. 3. Schematic illustrating the method of atomistic tensile test. (a) Movement of frozen layers of atoms by pulling, and (b) squeezing the simulation box throughout its length to simulate the atomistic tensile test. The solid arrows indicate the direction of applied force/strain and the dotted arrows indicate the direction of the developed response.

$$\sigma_{ij} = \frac{1}{V}\left\{ -m v_i v_j - \frac{1}{2}\left[\sum_{n=1}^{N_p}\left(r_{1i}F_{1j} + r_{2i}F_{2j}\right) + \sum_{n=1}^{N_b}\left(r_{1i}F_{1j} + r_{2i}F_{2j}\right)\right] - \frac{1}{3}\left[\sum_{n=1}^{N_a}\left(r_{1i}F_{1j} + r_{2i}F_{2j} + r_{3i}F_{3j}\right)\right] - \frac{1}{4}\left[\sum_{n=1}^{N_d}\left(r_{1i}F_{1j} + r_{2i}F_{2j} + r_{3i}F_{3j} + r_{4i}F_{4j}\right) + \sum_{n=1}^{N_i}\left(r_{1i}F_{1j} + r_{2i}F_{2j} + r_{3i}F_{3j} + r_{4i}F_{4j}\right)\right] - \text{Kspace}(r_{ki}, F_{kj}) - \sum_{n=1}^{N_f} r_{fi}F_{fj}\right\} \tag{10}$$

V is the volume, m is the mass, v is the velocity of an atom, r_{1i}, r_{2i}, r_{3i}, r_{4i}, r_{ki}, and r_{fi} are the positions of the atoms and F_{1j}, F_{2j}, F_{3j}, F_{4j}, F_{kj}, and F_{fj} are the forces on the atoms. The virial stress is equivalent to Cauchy stress which makes virial stress be used in MD simulations. The strain along the loading direction is calculated using the initial length $L(0)$ and instantaneous length $L(t)$ at time t as $\varepsilon(t) = (L(t) - L(0))/L(0)$. The temperature is maintained by a thermostat and the rate of deformation is controlled by the rate of change of box dimension. Since deformation is a dynamic process (NEMD), the stress–strain behavior changes as the system evolve obeying Newton's law.

The uniaxial test is a simple test from which important mechanical properties can be derived [33]. There are two common methods of doing the atomistic uniaxial tests at the nanoscale level using MD technique [10]. Fig. 3 illustrates the method of atomistic tensile tests with schematic images. Few layers of atoms on the top and bottom are frozen and pulled apart (as shown by the solid arrow in Fig. 3a) to resemble the tensile test [12,80]. The non-periodic boundary condition is applied to the loading direction and periodic boundary condition (PBC) is applied to the other two directions. The direction of the movement of the frozen layers of the atom is reversed to compress the material. After each movement step of the frozen layers of atoms, the atoms within the frozen layers are allowed to evolve using NVE ensemble. In a tensile simulation, atoms evolve by moving away from each other causing necking and failure of the material [12,81,82]. Fracture studies in the presence of crack use this method (Fig. 3a). Another method (Fig. 3b) is to squeeze the material throughout its length which leads to elongation along the other direction (as represented by the dotted arrows). This is done by constantly squeezing the material and using NPT ensemble [22] to move the atoms by Newton's law. This can also be visualized as a change in the box size to deform the material. PBC is applied in all directions. The interaction of dislocation with other dislocations, GB/interfaces, and precipitates are usually studied using this method. Necking is not observed in this method. There are similar works using NVT ensemble [57]. The rate of movement of the fixed layer of atoms or the rate of squeezing determines the strain rate. Boundary conditions play an important role in determining the mechanical properties in MD simulations. Non-PBC creates surfaces that act as nucleation sites for dislocations due to which the mechanical stress value required for dislocation nucleation is lower than when PBC was used [24]. These surfaces add extra energy to the configurations. These surfaces and non-PBC should be avoided while minimizing GBs and finding GB energy. In configurations with crack, the surfaces act as stress-rising areas along with the crack tip. In simulations with PBC, the mobile dislocation exit at the simulation box (say, at -x) and re-enter again into the simulation box (say, at +x), thus adding to the dislocation density calculation. In simulations with non-PBC, the mobile dislocation exit at the simulation box creating a step.

The initial strain contributes to the elastic stretching of bonds of the atoms [8]. Beyond an increase in the interatomic distance, the materials enter plasticity, but still maintaining a linear stress–strain relationship. There is no yield point seen in most of the studied atomistic configurations due to them either being defect-free or having a relatively smaller number of defects, impurities, and precipitates as compared to real-life materials. The absence of yield point is also due to the high strain rates obtained during the simulation. Thus the maximum stress value is preferably used over the yield stress [53]. Apart from this, there are various other properties (Young's modulus, shear stress, defect nucleation stress) which can be determined in a uniaxial simulation. The maximum stress during uniaxial simulation can be assumed to be the ultimate strength (referred here as simply strength) of the metals. The component of pressure tensor value (P_{ij} in equation (9)) or the component of stress tensor value (σ_{ij} in equation (10)) averaged over the number of atoms in the system can be used to calculate the stress value of the system. This value is plotted against the normal strain ($\varepsilon(t) = (L(t) - L(0))/L(0)$) to get the stress–strain behavior of the configuration. The maximum value of this stress achieved during simulation is referred to as 'maximum stress'. After the point of maximum stress, the potential energy of the system drops simultaneously as the stress drops, showing the formation and growth of voids, which was considered as failure in one of the works [53]. The

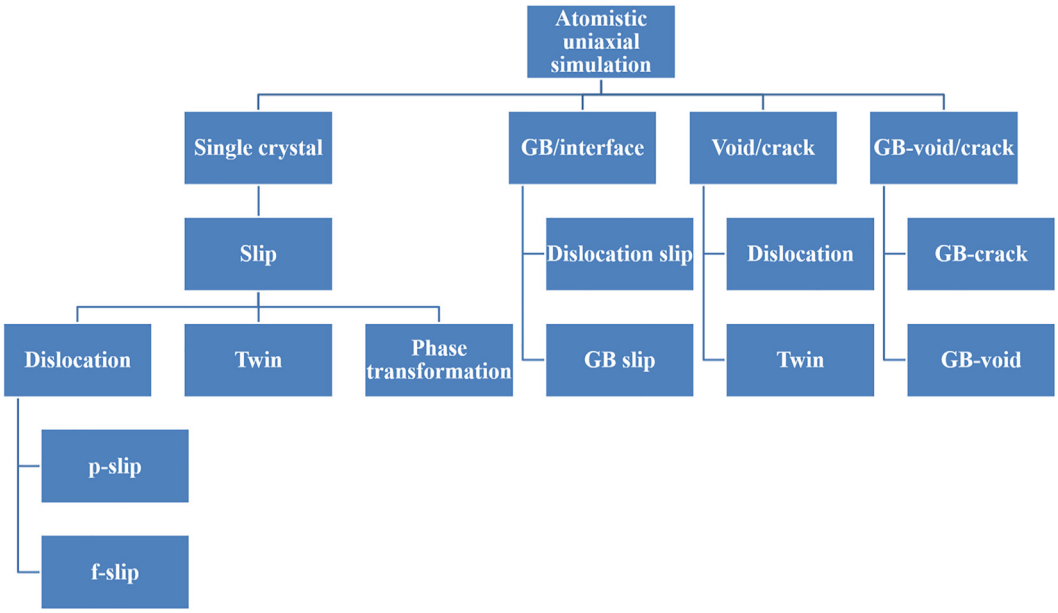

Fig. 4. Flow chart showing the outline of the current article.

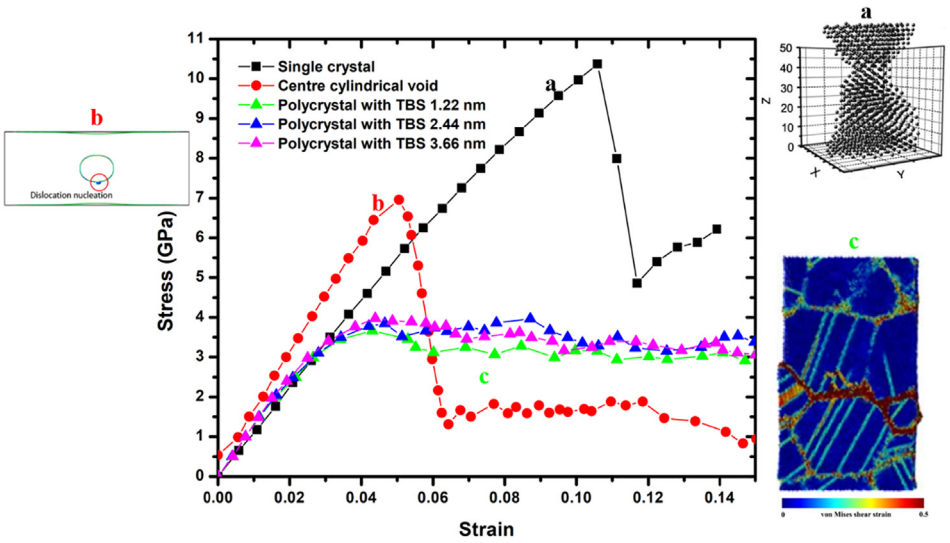

Fig. 5. The stress–strain plot of Ni configurations in uniaxial simulations. (a) Single crystal after initiation of necking. Reproduced with permission from reference [57]. (b) Point of dislocation nucleation in a single crystal with cylindrical void configuration. Atoms around the void and dislocation are only shown. Reproduced with permission from reference [87]. (c) Nanocrystalline with twin boundary spacing (TBS) of 1.22 nm. Atoms are colored using values of Von Mises shear strain. Reproduced with permission from reference [88].

difference in potential energy can be attributed to energy barriers for dislocation nucleation from a void or a crack tip or GB [83]. In earlier work, change in pair distribution function $g(r)$ was considered as failure of the material [22]. Initial characterization of the atomic arrangement was done using $g(r)$ and then using common neighbor analysis (CNA). Using CNA as base, Stukowski came up with technique to characterize defects [66,67]. One of which is dislocation extraction algorithm (DXA) [84] implemented in Open Visualization Tool (OVITO) [85] used to characterize dislocations. Another important visualization tool is Atomeye [86].

Atomistic uniaxial simulations have been used to study single crystal deformation, crack initiation and propagation, dislocation nucleation from void/crack and GB, and dislocation interaction with interfaces. The outline of reviewed topics related to deformation behavior using atomistic uniaxial simulations in this current article is shown in Fig. 4. Section 3.1. deals with the deformation of single crystal configuration. Schmid and non-Schmid factors influence initial slip in the crystal, but it is discussed along with topics dealing with partial and perfect dislocations slip. As the formation of partial and perfect dislocations and twin in a single crystal is similar to their nucleation from the crack tip, it is also explained with figures in Section 3.3. Section 3.2 deals with dislocation and GB slip in GB/interface and nanocrystalline configurations. Section 3.3 deals with nucleation of dislocations and twin from void/crack configurations. Section 3.4 deals with nanocrystalline configurations having void/crack with and without GB. GB-void/crack interaction is complex as compared to the configurations in previous sections and here the prediction of initial deformation behavior is presented.

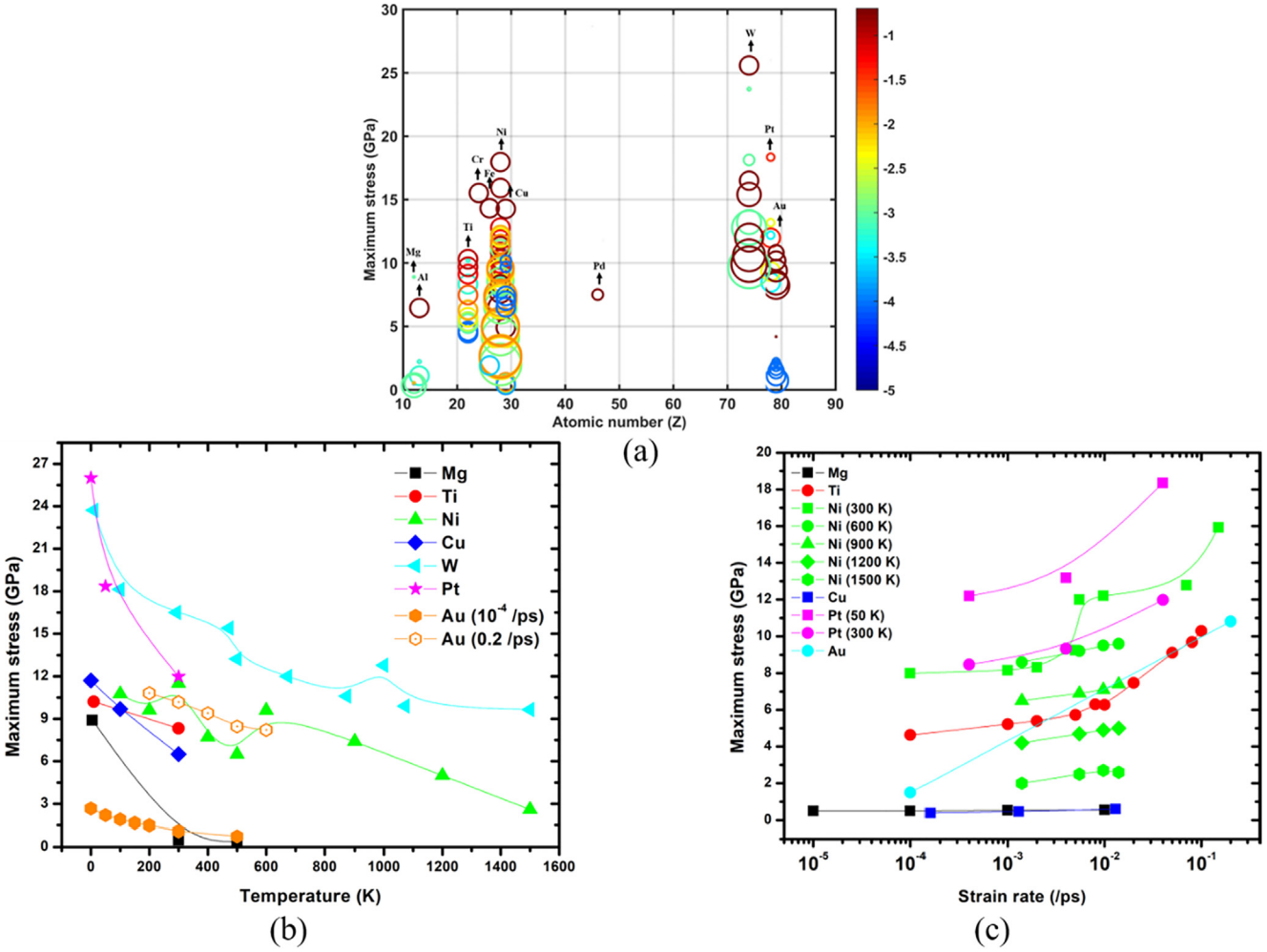

Fig. 6. The maximum stress values of single crystal configurations during uniaxial simulations. (a) The size of the circles corresponds to the temperature during simulations. The smaller circles correspond to the simulation carried out at a lower temperature and that of the larger circles at a higher temperature. The color of the circles corresponds to the logarithm of the strain rate (ps^{-1}). The maximum stress values of Mg, Ti, Ni, Cu, W, Pt, and Au are plotted as a function of (b) temperature and (c) strain rate. The values in the brackets in the legends of Fig. 6b and 6c represent the strain rates and temperatures of the simulations respectively.

One such set of atomistic uniaxial simulations shows the stress–strain plot of single crystal, void, and GB/interface configurations in Ni system at 300 K in Fig. 5 [57]. The stress–strain data points were collected from various literature sources at a common temperature of 300 K and almost near values of strain rate for Ni configurations. Single crystal configuration pulled at a strain rate of 5×10^{-4} ps^{-1} showed the highest maximum stress value. Point 'a' shows the configuration after necking has started. Single crystal with center cylindrical void configuration pulled at a strain rate of 5×10^{-4} ps^{-1} showed a lower maximum stress than that of the single crystal configuration. Point 'b' shows the nucleation of a dislocation from a void surface. Atoms immediately around the void and dislocation are shown and remaining atoms are made invisible for ease of visualization (Fig. 5b) [87]. Nanocrystalline configurations with twins of different spacing within the grains under compression at a strain rate of 10^{-3} ps^{-1} showed the least maximum stress value in the plot [88]. Twin boundary spacings (TBS) of 1.22, 2.44, and 3.66 nm are plotted to show the effect of TBS. The flow stress of the plotted TBS configurations is almost similar but the configuration with TBS of 3.66 nm is higher than the rest of TBS configurations. Point 'c' shows the intergranular damage caused during compressive loading at a strain of 0.08. The atoms are colored using Von Mises shear strain. The variation in maximum stress values of various configurations matches well with the schematic illustration in Fig. 2. A detailed deformation behaviour of single crystal configurations in the presence of GBs/interfaces and voids/cracks is followed hereafter in the Sections 3.1 to 3.3.

3.1. Single crystal configurations

Deformation and processing of single crystals and nanocrystals have gained interest in the application of structural, functional [12,54], and electronic materials [61,82,89–91]. The first step towards simulating the deformation of a single crystal configuration is to choose an orientation and deformation condition such as loading direction, temperature, and strain rate. Deformation of single crystal along various crystallographic directions showed that pulling along close-packed directions resulted in less strength as compared to pulling along the less packed directions [24,56]. The simulations with loading directions as ⟨100⟩ for BCC and FCC, and as ⟨0001⟩ for HCP are chosen from the literature. The influence of aspect ratio on strength of single crystal nanowire is observed [92] but it is not discussed in this article. Length does not influence the strength of single crystal nanowires directly while strength increases linearly with an increase in diameter [93]. Table 1 lists the maximum stress values of various single crystal configurations and their deformation conditions. Fig. 6a shows

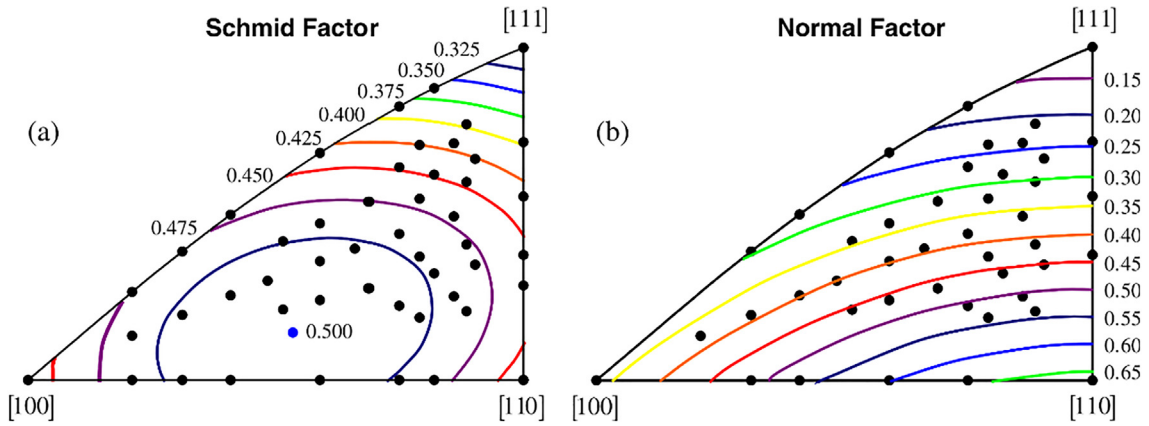

Fig. 7. (a) Schmid and (b) Non-Schmid (normal) factors for different orientations in FCC crystal. Reproduced with permission from reference [24].

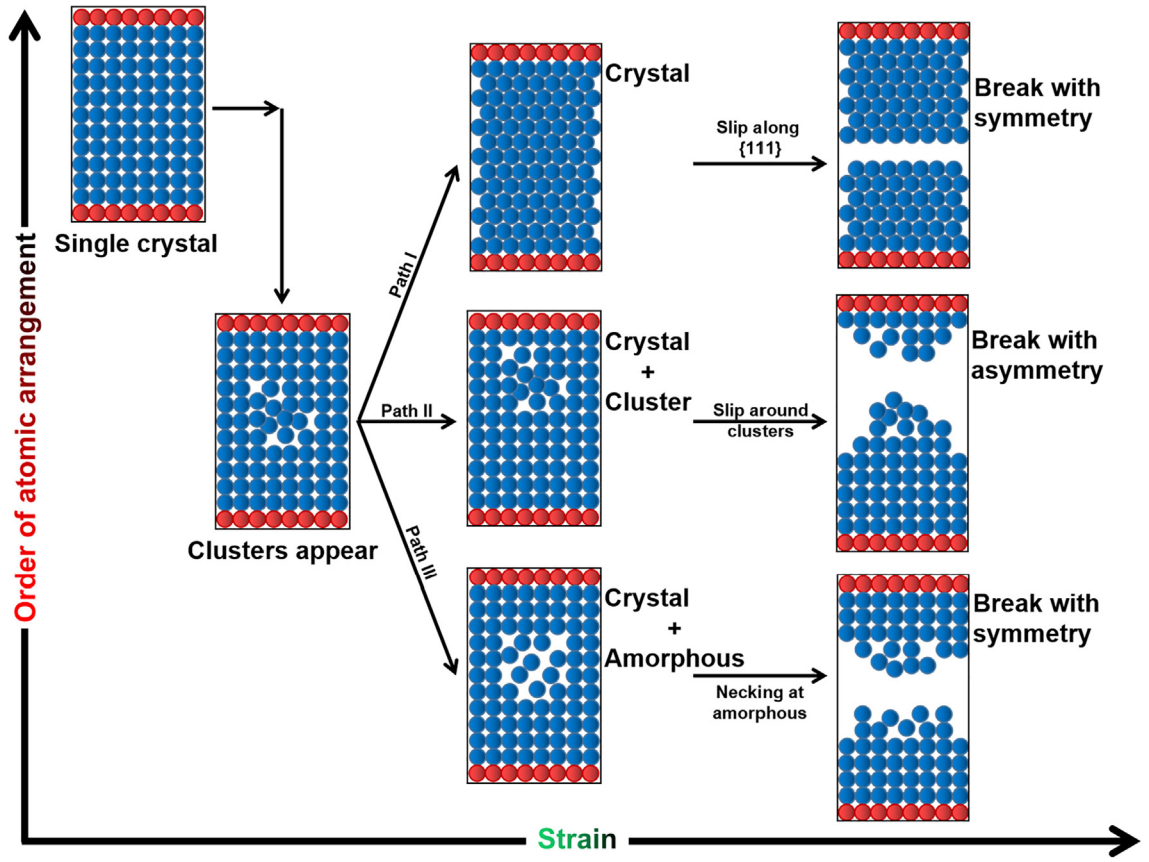

Fig. 8. Schematic illustration of the failure of single crystal configuration taking three distinct paths depending on the strain rate. Path I is a low strain rate case, path II is an intermediate strain rate case and path III is a high strain rate case. The red-colored atoms represent frozen atoms and the blue-colored atoms represent mobile atoms, which is similar to the configuration shown in Fig. 3a. Adapted with permission from [82]. Copyright (2007) American Chemical Society. (For interpretation of the references to color in this figure legend, the reader is referred to the web version of this article.)

the plot of maximum stress during uniaxial simulations (values from table 1) and the atomic number of metallic systems. The maximum stress values of Mg, Ti, Ni, Cu, W, Pt, and Au are plottedas a function of temperature and strain rate in Fig. 6b and 6c respectively. The following are a few observations made from Table 1 and Fig. 6. A good range of temperature and strain rate for varied metals were found in the literature, but there are still a lot of metals on which atomistic simulations are yet to be carried out. An increase in the temperature decreases the strength (Fig. 6b) and an increase in the strain rate increases the strength (Fig. 6c). This shows the interplay of temperature and strain rate on the strength of the single crystal configurations. More MD studies on the dependence of strength on temperature and strain rate can be found in these references [79,81,90,94,95]. In simulations done at 0 K, the aim was to study the effect or behavor of a particular defect (such as dislocation, GB, void/crack) devoid of any effect of temperature. The aim of the simulations carried out at various temperatures was to study the transition of properties with temperature. Deformation of platinum and iron nanowires showed a change from brittle to ductile fracture when the temperature was increased [79,96].

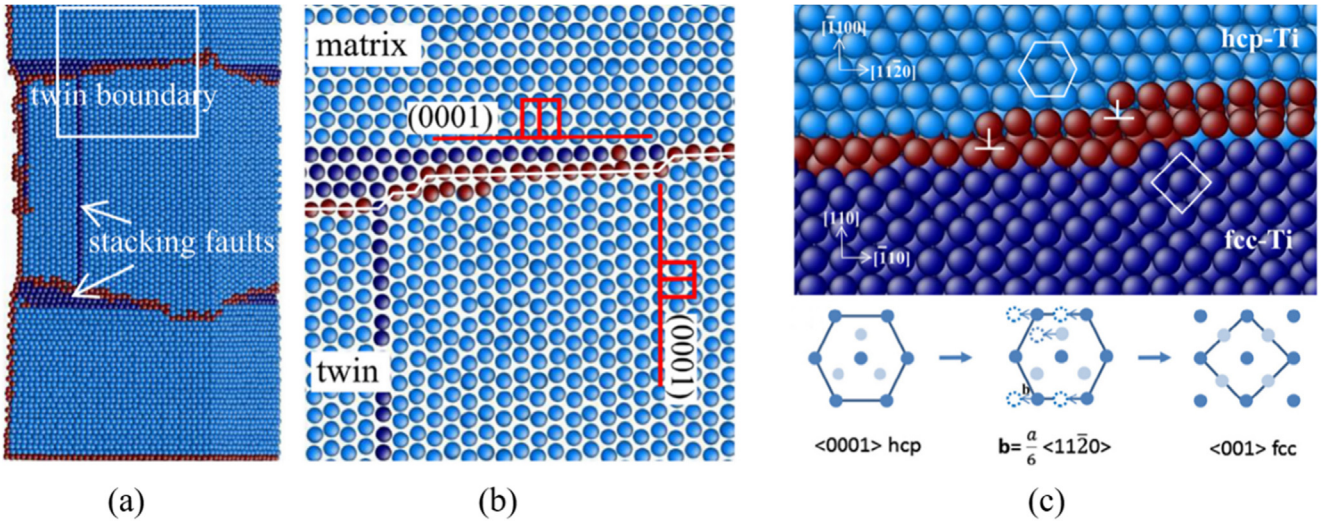

Fig. 9. (a) Twinned region and SFs between the twin boundaries are marked. (b) Zoomed images of the twin boundary from the box in (a) show a matrix-twin orientation relationship. (c) HCP to FCC transformation with orientation relationships shown in each phase with the partial dislocations at the phase interface. A schematic illustration of the transformation is shown beneath the atomistic image. Reproduced with permission from reference [102].

Dislocation nucleation stress decreases as temperature increases [97]. In BCC tungsten above 673 K, twin bands slip in two directions of {110} planes as compared to the usually observed slip in one direction in FCC metals [98]. Table 1 has the data from the following references [6,53,57,59,61,63,75,79,80,82,89,90,98–126].

3.1.1. Schmid and non-Schmid effects

Single crystals deform by the slip of atoms on a particular plane and direction having the highest Schmid factor. Non-Schmid factor also contributes to slip in certain cases [24]. MD simulations have shown that the nucleation of partial and perfect dislocations in a single crystal configuration is dependent on both Schmid and non-Schmid (normal stress component) factors. Non-Schmid factor has the same formulation as the Schmid factor but here the normal stress component on the plane instead of the shear stress component is considered. The normal stress to the glide plane is equal to the non-Schmid factor multiplied by the externally applied stress.

The stress required for homogeneous nucleation of partial dislocations in various oriented single crystal configurations is calculated using PBC in MD simulations. Non-PBC bring in a surface effect that result in nucleation of dislocation from the surface, something which is undesirable. The loading directions for various single crystal orientations are shown as points in the standard stereographic triangle with [100], [110], and [111] as vertices (Fig. 7) [24]. Values of Schmid and non-Schmid factors are shown as a gradient of rainbow colors and values marked to them. Maximum Schmid and non-Schmid factors for FCC crystals of various orientations were 0.5 and 0.65, respectively. This shows the contribution of the non-Schmid factor to dislocation nucleation.

3.1.2. Strain rate effects

The initial stage of slip causes changes in the local atomic arrangement. The behavior of the atoms on the slip plane is dependent on the strain rate. Wang et al. [82] summarized the work of Koh et al. [79,81] with different strain rate simulations showing three distinct paths of failure, according to the local changes in the atomic arrangement referred to as clusters (Fig. 8). A cluster is a group of atoms with differing atomic arrangements or a different number of neighbors than the original atomic configurations, and is of a few nanometers in size. Fig. 8 shows that the failure of a single crystal can take three paths depending on the strain rate [82]. In all three paths, a small volume of the single crystal transforms to clusters during the initial strain. With further straining,

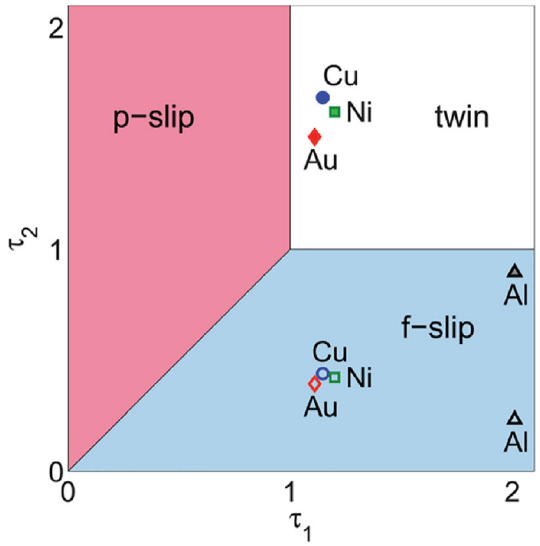

Fig. 10. Deformation mechanisms of FCC nanowires modeled using two parameters τ_1 and τ_2. Open symbols represent tensile along ⟨100⟩, compression along ⟨110⟩ and ⟨111⟩ loading conditions. Filled symbols represent compression along ⟨100⟩, tensile along ⟨110⟩ and ⟨111⟩ loading conditions. Three regions were marked as slip by full dislocations (f-slip), slip by partial dislocations (p-slip), and twins. Reproduced with permission from reference [135].

the system takes three different paths depending on the strain rate. Part I is at lower strain rates where clusters slip on the preferred plane and eventually fail at the central portion of the simulation box. Path II is at intermediate strain rates, where clusters transverse throughout the length of the nanowire and fail near the end of the wire [127]. Path III is at higher strain rates where clusters transform into an amorphous phase and then fail in the middle part. This was later observed in titanium single crystal deformation [107]. It can be seen that in a low strain rate (0.016% ps^{-1}) simulation, the atomic arrangement is ordered when compared to high strain rate simulation (1.3% ps^{-1}).

3.1.3. Movement of partial dislocations and twinning

From Wang and Koh's work, there is evidence of change in atomic arrangements during the uniaxial simulation. However,

there was a lack of information on the nucleation of clusters and the amorphous phase. Following them, researchers have attributed the change in atomic arrangement to dislocations, twins, and phase transformations [102,128,129]. There is a competition between (partial and perfect) dislocations and twins, which is discussed at the end of this section. Tschopp [24] showed the nucleation of partial dislocations in single crystal copper. Some researchers have attributed the atomic rearrangement to phase transformation [128,130–132]. Ma et al. [98] showed phase transformation in tungsten nanowire during tensile deformation. Ren et al. [102] showed that the movement of partial dislocations in the twinning region induced HCP to FCC transformation (Fig. 9a and 9b) with orientation relationships of $\langle 0001\rangle_{hcp}||\langle 100\rangle_{fcc}$, $\langle 01\bar{1}0\rangle_{hcp}||\langle 0\bar{1}1\rangle_{fcc}$, and $\langle 2\bar{1}\bar{1}0\rangle_{hcp}||\langle 011\rangle_{fcc}$ as seen in the Fig. 9c. Similar works on phase transformation such as FCC → BCC → HCP [20], BCC → HCP [131], FCC → HCP [128] can be found in the reference. The nucleation of the twin embryo can be seen in the reference [102,107]. Rawat et al. [64] observed that twinning does not evolve throughout the simulation box, but wherever it does, it helps in phase transformation, which is similar to the observations of Ren et al. [102]. From the above results, it can be seen that if the deformation mechanism in a single crystal configuration is through phase transformation, then the configuration undergoes the following steps – partial dislocation slip → twin embryo → twin growth → phase transformation. The leading partial dislocation can also combine with its trailing partial dislocation to form a perfect dislocation in a single crystal due to surface effect if the width of the stacking fault (SF) is less than 19 nm [133]. The width of the simulation box brings in the surface effect which affects the deformation mechanism of the single crystal configurations. The width of the configuration below which the strength increases with increase in width and above which the strength decreases with increase in width is called the critical width. So, it can be interpreted that a single crystal with a width higher than the critical width allows partial dislocations to form a twin embryo. It also requires the trailing partial dislocation to be on a similar adjacent plane to the leading partial dislocation to form a twin. Simulation box with width less than the critical width undergoes the following step – partial dislocation slip → perfect dislocation slip and controlled by dislocation slip as deformation mechanism. A similar mechanism is seen in the crack configuration (Section 3.3) where the crack tip and its orientation affect the mechanism.

Twinnability is the ability of the material to deform by twinning rather than by slip [134]. Twinnability parameter could not be used to explain the competition between (partial and perfect) dislocations and twins because of its inability to distinguish perfect and partial slip and twinning. Weinberger and Cai compiled the plasticity of FCC nanowires showing the importance of SFEs in the nucleation of dislocation and twin as shown in Fig. 10 [135]. They used SFEs of intrinsic, unstable SFs and unstable twinning energy of various FCC metals to calculate the parameter τ_1 the ratio of critical stress for the activation of partial slip to that for twinning. Along with the SFE values, Schmid factors of partials are used to calculate τ_2 the ratio of critical stress for perfect dislocation slip to that for twinning. τ_1 and τ_2 parameters are intrinsic to the metal and have a similar formulation to the twinnability parameter. The two parameters τ_1 and τ_2 are formulated in terms of SFEs as:

$$\tau_1 = \frac{\gamma_{USF}}{\gamma_{UT} - \gamma_{ISF}} \tag{11}$$

$$\tau_2 = \frac{\gamma_{USF} - \gamma_{ISF}}{\gamma_{UT} - \gamma_{ISF}} * \frac{S_{lead}}{S_{trail}} \tag{12}$$

where γ_{ISF}, γ_{USF}, and γ_{UT} are the (intrinsic) SFE, unstable SFE, and unstable twinning energy respectively. SFE can be calculated using ab initio calculations and molecular static simulations with the SF structure modeled in the system. Both stable and unstable SF play an important role in the deformation mechanism [136]. S_{lead} and S_{trail} are the Schmid factors of the leading and trailing partial dislocations which can be calculated using a method similar to that proposed by Tschopp [24]. Plotting those two parameters (τ_1 and τ_2) showed three domains depending on the mechanism of deformation (Fig. 10). Domain f-slip denotes slip by perfect dislocations, domain p-slip denotes slip by partial dislocations, domain twin denotes twinning. Both parameters τ_1 and τ_2 need to be high for twinning to occur. However, due to constraints from orientation and loading factors, it is difficult for the formation of partial dislocation (p-slip) and eventually twin. High SFE favors formation of perfect (full) dislocation (f-slip) even though the Schmid factor does not favor f-slip. The result shows that twinning is possible in compression loading along ⟨100⟩, and tensile loading along ⟨110⟩ and ⟨111⟩ in FCC crystals, except in case of aluminum due to its high SFE [137]. Copper is at the top and aluminum is at the bottom of the twin domain, indicating the high probability of twinning in copper due to its low SFE as compared to aluminum.

3.2. GB/interface configurations

3.2.1. Grain boundary type

GBs play an important role in strengthening materials. Their strengthening efficiency depends on the GB type and arrangement of atoms in the GBs [138,139]. GB types are characterized by the tilt [139], twist [140], and twin [141] boundaries, where each of these are defined by the symmetrical or asymmetrical angles the grains make with the adjacent grain. The initial step is to model the GB by finding the crystallographic orientations of the grains [142] and decide the center of the grain. With these details, bicrystals to polycrystals can be modeled [143–146]. The GB and nanocrystalline configurations are equilibrated to get to a minimum energy configuration. The equilibrated GB region consists of structures that are different from usual unit cells in the grain. The GB structures can be explained using seven Bernal structures [147]. The structures can vary in the GB depending on the angle of the tilt or twist or twin of the grains. The GB energy depends on the GB structure. The maximum coincidence of lattice sites of the two grains in the GB region creates low energy structures and are referred to as coincident site lattice (CSL) GBs or Σ GBs. Low angle GBs (LAGBs) and Σ GBs exhibit low GB energy and high strength [139]. The maximum stress in the atomistic uniaxial simulation of GB configurations is seen during the nucleation of dislocation from the GB structure. The equilibrated configuration before deformation will have no or negligible stress. During deformation, the kinetic energy of the atoms increases which contributes to the virial stress calculation. The stress rises due to change in the number of neighboring atoms, bond breakage, dislocation generation, and external applied strain or force. Thus, the calculated stress includes the stress contributions from all the atoms including the atoms at the GB and this stress increases slowly as the configuration is strained. Fig. 11a shows the plot of the maximum stress of GB/interface configurations during uniaxial simulations (values from Table 2) and the atomic number of metallic systems. The maximum stress values of Fe, Ni, and Au are plotted as a function of GB spacing in Fig. 11b. Table 2 has the data from the following references [88,113,118,123,141,148–150].

Deformation of bicrystal configurations can be used to study the emission of partial and perfect dislocations from GBs [141,142]. During the deformation of GB configurations, the GB structure changes at lattice sites where the number of neighboring atoms changes (CNA) and symmetricity around the atomic sites reduces. This loss in symmetry and the number of neighbors around each atom in the GB structure is called dissociated structure. Equili-

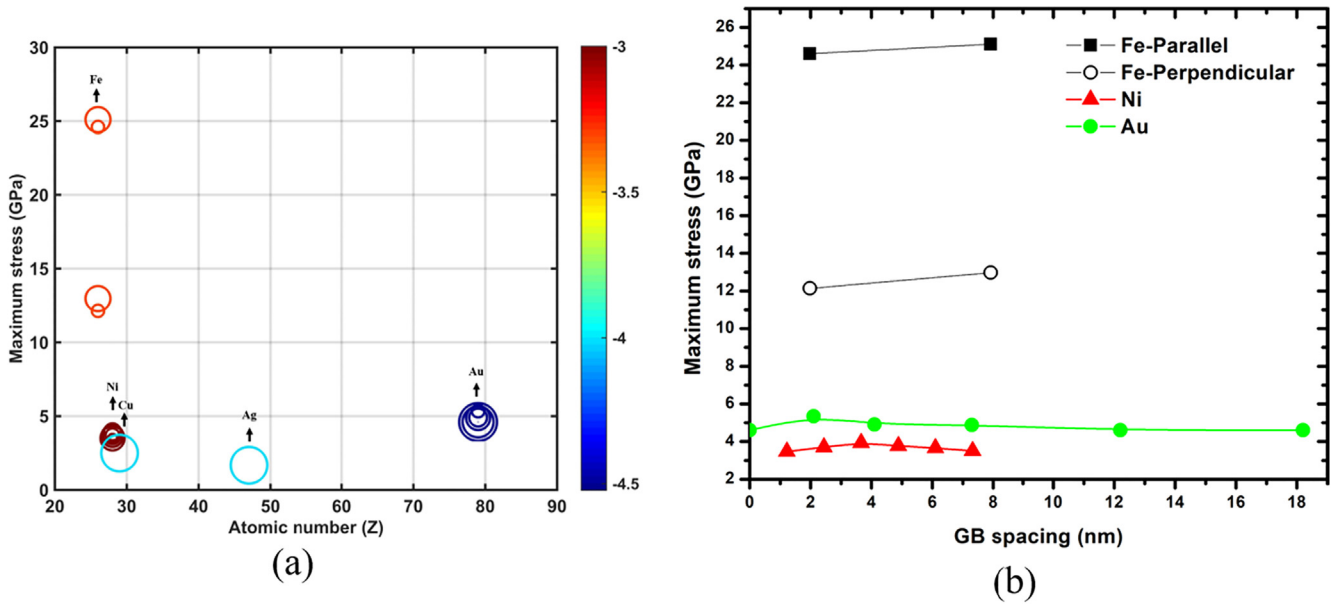

Fig. 11. The maximum stress of GB/interface configurations during uniaxial simulations. (a) The size of the circles corresponds to the interspacing between the GB/interfaces in the simulations. The smaller circle corresponds to the configurations with a lesser number of interfaces and that of the larger circle with a large number of interfaces. The color of the circles corresponds to the logarithm of the strain rate (ps^{-1}). (b) The maximum stress values of Fe, Ni, and Au are plotted as a function of GB spacing. The variation in maximum stress values in Fe is due to the direction of pulling represented as parallel and perpendicular to the GB plane.

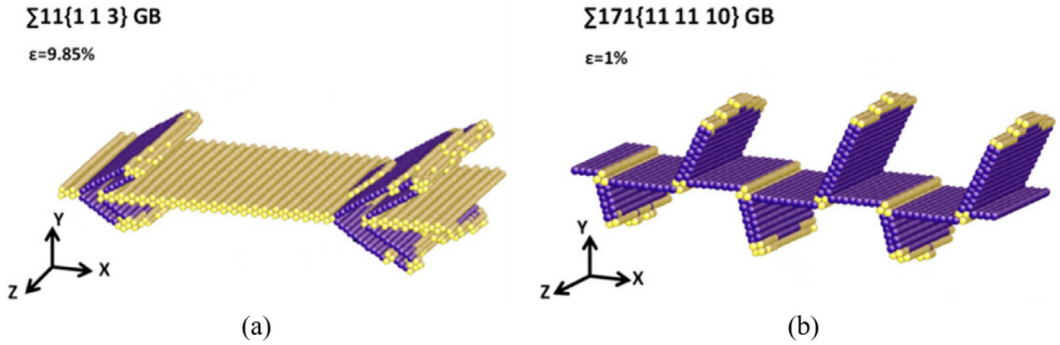

Fig. 12. Dislocations nucleation from copper GB configurations in an atomistic uniaxial simulation (a) Σ 11 GB and (b) Σ 171 GB configurations. Only the atoms in the GB region and at dislocations nucleating from the GB are shown after CNA. The yellow-colored atoms represent the GB region and dislocation core. The blue-colored atoms represent SFs. Reproduced with permission from reference [83]. (For interpretation of the references to color in this figure legend, the reader is referred to the web version of this article.)

brated non-CSL high angle GBs (HAGBs) can be assumed to have a dissociated structure in the GB region [142]. Dislocations nucleate from these dissociated structures at a particular stress value called critical stress for dislocation nucleation. The critical stress required to emit dislocations from a particular GB type is constant [151] and is discussed in Section 3.4. HAGBs have dissociated structures, which makes them high energy configurations. This causes them to deform at lower strain and stress values, and so making the critical stress for dislocation nucleation low. LAGBs and Σ GBs have a less dissociated structure as compared to HAGBs, thus making them comparatively more difficult to deform. There were observations of Σ 3 GBs deforming at higher strains and the nucleation of lattice dislocations occurring more willingly than that from the HAGB [83]. Within all the Σ GBs, the Σ 3 GBs has the least GB energy. Fig. 12 shows two Σ GB configurations emitting dislocation when pulled along Y-direction. The strain at the point of dislocation nucleation is shown at the top left corner in the figure. It can be seen that dislocation nucleation from Σ 11 GB happened at 9.85% strain while the dislocation nucleation from Σ 171 GB happened at 1% strain itself. The partial dislocations (observed as creation of SFs) nucleating from Σ 11 GB and from Σ 171 GB can be seen in Fig. 12a and 12b respectively.

3.2.2. Influence of boundary spacing

The difference in the deformation behavior of bicrystals and nanocrystalline configurations is due to the difference in the GB/interface interspacing distance. Grain size at the microscopic length scale influences material strength through GB strengthening following the Hall-Petch equation. Researchers have shown an inverse Hall-Petch relation in nanocrystalline configurations with a change of deformation mechanism from dislocation activity to GB sliding [152]. Deformation of nanocrystalline configurations can be used to study intergranular and intragranular fracture [145,153] (similar to Fig. 5c [88]), dislocation nucleation and activity, and GB deformation [152]. GBs act as nucleation sites for dislocations and can thus be thought of as a source of dislocations. The uniaxial stress–strain response and the maximum stress observed during atomistic simulations of various materials with nanocrystalline configurations are governed by multiple factors such as texture, GB types and their number fraction, grain size, and the

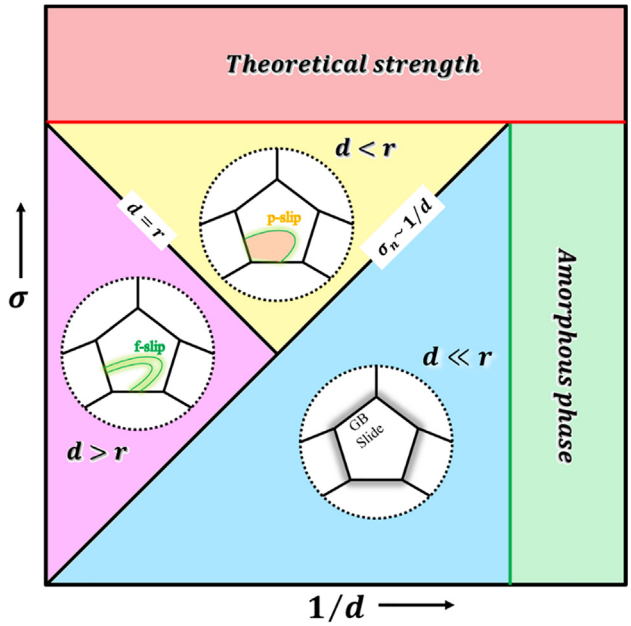

Fig. 13. Schematic illustration of the atomistic deformation mechanism map of nanocrystalline metals adapted from reference [76]. The red-colored region represents theoretical strength, the pink-colored region represents the activity of full dislocation (f-slip), the yellow-colored region represents the activity of partial dislocation (p-slip), the blue-colored region represents GB deformation, and the green-colored region represents the amorphous phase. The transition from one mechanism to another is separated by black-colored lines. (For interpretation of the references to color in this figure legend, the reader is referred to the web version of this article.)

number of grains within the simulation box [154]. The difference in maximum stress during compression and tensile atomistic simulations in single crystal configurations arises due to asymmetry in friction between the neighboring {112} planes in BCC systems [106,129]. Asymmetry in tension–compression in metals can also be influenced by screw dislocations exhibiting non-planar structure [155,156]. However, in nanocrystalline configurations, along with the above factors, grain size also influences the tension–compression asymmetry [157]. The nucleation stress σ_n of a dislocation inside a grain of size d is given by equation (13) [76]. In nano length scale, the distance between the interfaces/GBs influence the material strength but by a different deformation mechanism. The mechanism operating at nanoscale is given by equation (14) and schematically shown in Fig. 13 [76].

$$\sigma_n = \sigma_0 + \frac{k}{\sqrt{d}} \tag{13}$$

$$\sigma_n \sim \frac{1}{d} \tag{14}$$

Here σ_0 is the yield stress of single crystal and k is a constant dependent on the GB strength. The nucleation stress is inversely proportional to the grain size in nanocrystalline materials. To demarcate the deformation mechanism at the nanoscale level, the plot between resolved shear stress (σ) and inverse grain size ($1/d$) shows three regions depending on the value of grain size and dislocation splitting distance (Fig. 13) [76]. Dislocation splitting into partials separated by a distance is denoted by $r = \frac{r_0}{1-\sigma/\sigma_\infty}$[76], where σ_∞ is the resolved shear stress when the splitting distance of the partials becomes infinitely large and r_0 is the equilibrium splitting distance when the resolved shear stress is zero. From the relation between r and r_0, both these variables can be used to compare with d. In nanoscale configurations, d can also be the interspacing distance between two interfaces or GBs [141]. For all values of grain size, there exists a resolved shear stress so high that it reaches theoretical shear strength ($G/2\pi$) of the material (red-colored region in Fig. 13). When grain size is reduced to nanosize but higher than the splitting distance, then perfect dislocation slip (f-slip) can be observed in the region ($d > r$). The grain size is large enough to accommodate leading and trailing partial dislocations and allowing the formation of perfect dislocation within the grain as seen in pink-colored region in Fig. 13. When the grain size is reduced further $d < r$, partial dislocation slip (p-slip) is prominent (yellow-colored region in Fig. 13). The transition from perfect to partial dislocation slip is marked by $d = r$ line. For $d \ll r$, the possibility of dislocation nucleation is low and GB deformation becomes prominent which includes GB diffusion and GB sliding (blue-colored region in Fig. 13). The transition from dislocation slip to GB deformation is marked by $\sigma_n \sim 1/d$ line. For $r_0/d > 1$, the configuration loses its crystallinity and becomes amorphous and the concept of crystal plasticity fails (green-colored region in Fig. 13).

3.3. Void/crack configurations

Voids and cracks cause catastrophic failure of structural materials. Crack growth or failure is because of the rupture and breakage of interatomic bonds [8]. The information about their initiation and propagation within the grain or at the interface is important [7]. MD can be used to study the deformation of porous materials with porosity at the nanoscale [158]. In a pristine configuration, the failure starts by nucleation of voids, their growth, and coalescence as widely seen in ductile fracture[159]. In contrast, in brittle fracture, the voids grow ahead of or with in the pre-existing crack causing catastrophic failure [35]. Void can be differentiated from the crack, in its formation, dimension, shape, and mode of failure caused by them. Voids can be formed from vacancy clusters [160], at the interface between the second particle and matrix, and ahead of the crack tip [160,161] while cracks can be formed from voids [87]. Voids are three-dimensional defects while crack surfaces in most of the configurations are assumed to be planar defects [35]. Aghababaei et al. considered a spherical defect of 2 nm diameter as void and a square region of 2 nm × 2 nm and an atomic layer thick as crack [103] and a similar differentiation between void and crack was presented by Li [162]. Under the same loading conditions, the crack showed a higher growth rate than the void [162]. These are the differences found between the void and crack in the literature. The characteristics of the void and crack configurations are given in the first column of table 3. In crack configurations, the maximum stress is observed just at crack blunting. The maximum stress of single crystal configurations in the presence of void/crack during atomistic uniaxial simulations (values listed in table 3) is plotted against the atomic number of various metals in Fig. 14a. In Fig. 14a the void diameter and crack length are represented by the size of the circles. The larger circles sizes represent configurations with large crack length or void diameter. The maximum stress values of Al, Ni, Cu, and Ta are plotted as a function of void diameter or crack length, temperature, and strain rate in Fig. 14b, 14c, and 14d respectively. It is seen that the configurations with larger void/crack had less strength. Table 3 has data from references [35,63,87,103,111,118,122,150,159–171].

The plastic zone around the void takes an annulus shape while the butterfly-shaped plastic zone is observed around the crack tip [172]. Dislocation emission from void or crack increases the toughness. Dislocation emission is always seen in void configuration due to the annulus shape of the plastic zone and thus inherent toughening in the void configuration is observed. Dislocation emission or cleavage mechanism of crack propagation depends on the orienta-

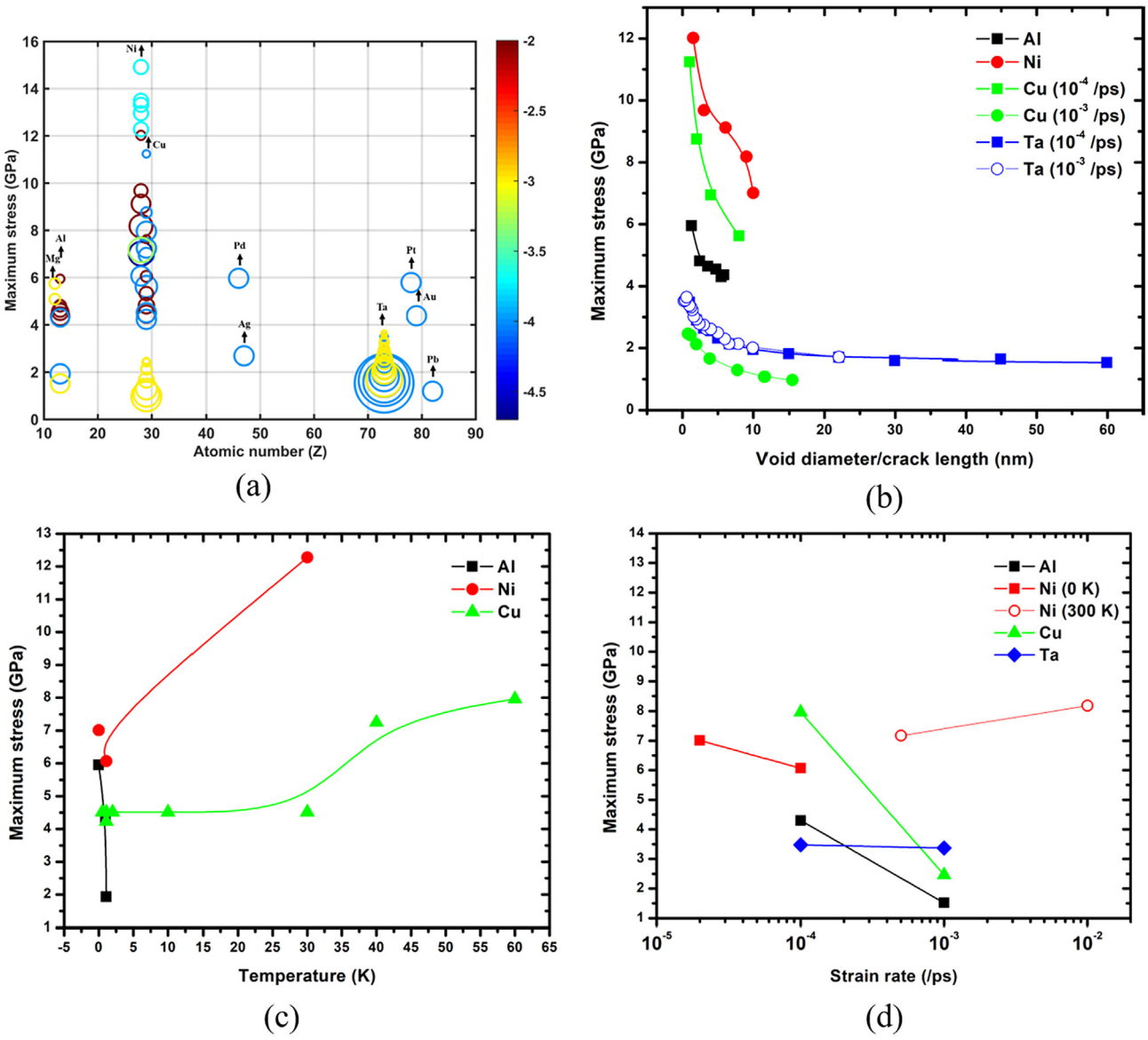

Fig. 14. The maximum stress of single crystal configurations in the presence of void/crack during uniaxial simulations. (a) The size of the circles corresponds to the void/crack size. The smaller the circle the smaller the void/crack and vice versa. The color of the circles corresponds to the logarithm of the strain rate (ps^{-1}). The maximum stress values of Al, Ni, Cu, and Ta are plotted as a function of (b) void diameter or crack length (c) temperature and (d) strain rate. The values in the brackets in the legends of Fig. 14b and 14d represent the strain rates and temperatures of the simulations respectively.

tion of the crystal [173] and microstructural features ahead of the crack [165,166,174], thus changing the toughening mechanism. Brittle cleavage fracture is observed if the angle between the crack plane and the close-packed plane of the crystal is within 16° and dislocation emission followed by ductile fracture is observed if the same angle is between 16° and 90° [160]. When the aspect ratio of the void changes, increase in void volume is observed; while during crack blunting, increase in its length is observed [159]. Dislocation loop emits from the void while dislocation line was observed to emit along the surface of the crack tip [164]. Crack blunting is observed due to the nucleation of dislocation, slip band, phase transformation [139,175,176] or twinning [177,178] from the crack tip [10,51,56,143].

The stress field at the crack tip is different during dislocation nucleation and phase transformation ahead of the crack tip and can be used to characterize the mechanism [179]. Using continuum mechanics the prediction of the stress at the crack tip becomes difficult, while atomistic studies have shown stress distribution from the first atom at the crack tip [10,26,180]. The deformation of single crystal configurations in the presence of a void of radius R is illustrated in Fig. 15 [159]. The mechanism for dislocation nucleation from the void is the same for spherical and cylindrical voids. The deformation of configuration with a cylindrical void is also shown in Fig. 5b [87]. First, dislocation nucleates at 45° with the tangent (tangent is not shown in the figure) of the void, which is the maximum shear stress (τ_m) plane (Fig. 15a, 15b, and Fig. 16). Fig. 16 shows side and top view of dislocation nucleation from void surface (initial void radius is 3.3 nm) from a MD simulation result [159]. Further deformation bends the dislocation to form a loop with radius R_1 (Fig. 15c). The stress required to nucleate the dislocation from the void consist of two components. One component contributes (τ_a) during nucleation by creating surface step [181] and the other component (τ_b) contributes during bowing [182] to move it to a particular distance ρ.

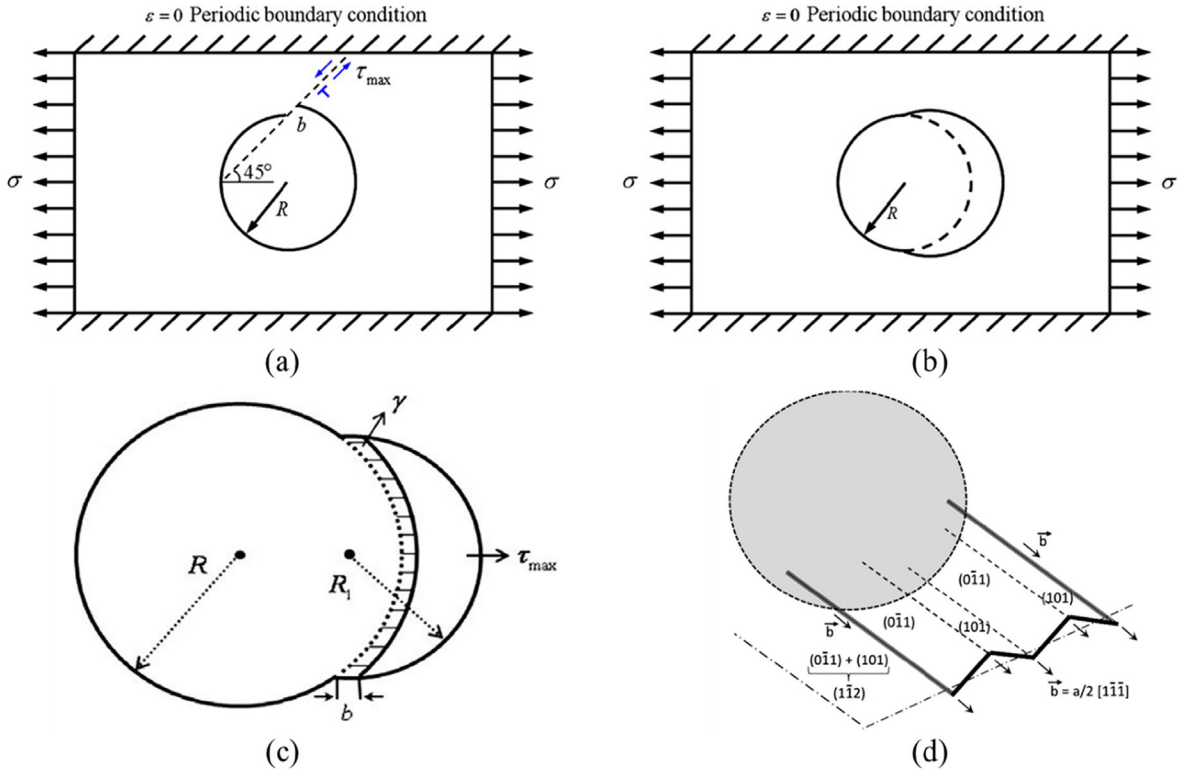

Fig. 15. Schematic illustrations of single crystal configuration with void (sphere) of radius R emitting dislocation with burger vector $\boldsymbol{b}$ during the uniaxial simulation. (a) side view showing nucleation of dislocation at 45° with the tangent (tangent is not shown in the figure) of the void which is the maximum shear stress (τ_m) plane, (b) top view, (c) top view of the void showing the formation of dislocation loop of radius R_1 by creating a surface step with energy γ. Reproduced with permission from reference[159]. (d) Ruestes schematically showed the reason for the curving of the nucleated dislocation from the void [183]. Dislocations moving on {110} planes with common burger vector $\boldsymbol{b}$ combine to slip on {112} plane. The screw part of the dislocation cross-slips and forms a loop. Reproduced with permission from reference [183].

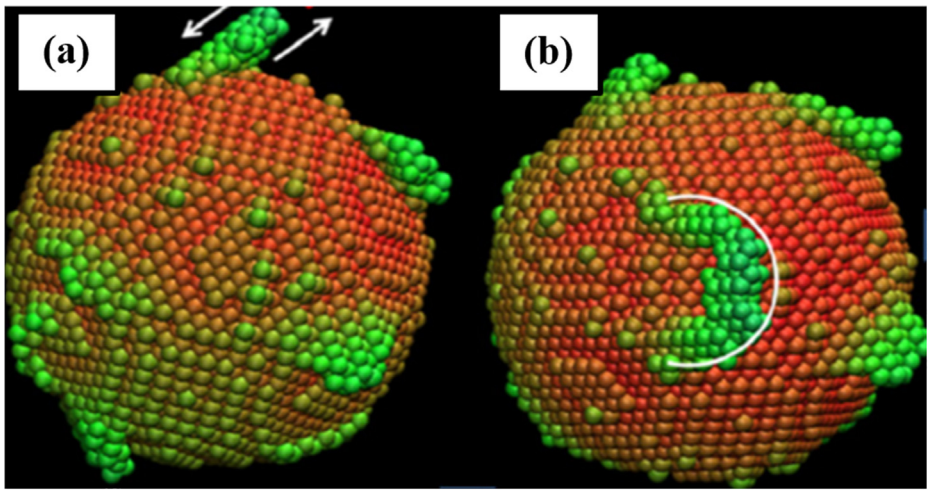

Fig. 16. (a) Side and (b) top views of dislocation loop initiation from the void surface in tantalum. The initial void radius is 3.3 nm. Shear stress direction is shown in the side view (a). Immediate atoms around void and dislocations are shown. Atoms are colored as per the distance away from the void center. Reproduced with permission from reference [159].

$$\tau_a = \frac{2\gamma}{\pi\rho\boldsymbol{b}} \tag{15}$$

$$\tau_b = \frac{G\boldsymbol{b}(2-\nu)}{4\pi(1-\nu)R_1} ln\frac{8mR_1}{e^2\rho\boldsymbol{b}} \tag{16}$$

γ is the surface energy per unit area creating a step for dislocation with burger vector $\boldsymbol{b}$, G is the shear modulus, ν is the Poisson ratio in a particular direction, m is a contact depending on the type of loops, and e is the exponential function [182]. Tang [159] showed using MD simulation that $R_1 = R/2$. Formation of loop from void in BCC is schematically illustrated by Ruestes [183] in Fig. 15d. Dislocations on the {110} planes with common burger vector $\boldsymbol{b}$ combine to slip on the {112} planes. The screw part of the dislocation can cross-slip and form a loop. The first component (τ_a) doesn't depend on the void size and so the stress required to nucleate the dislocation is almost same when the void size is less than 10 nm. When the void size is less than ~ 0.5 nm, heterogeneous nucleation

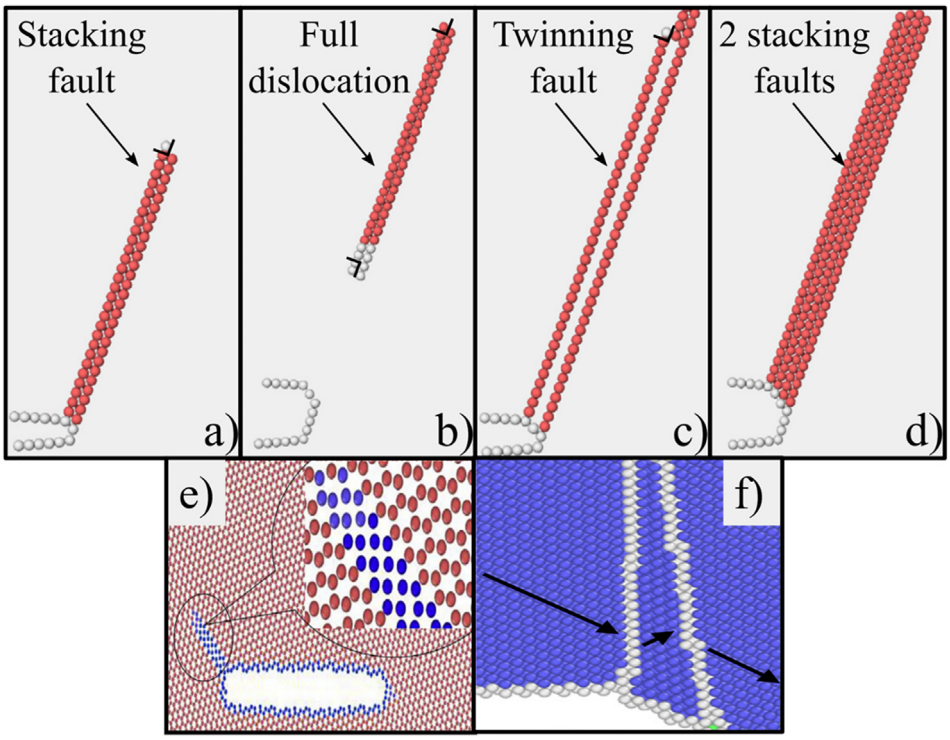

Fig. 17. (a-d) Crack-tip activity in FCC metals. (a) Nucleation of leading partial dislocation from the crack tip leaving behind a fault. (b) Nucleation of trailing partial dislocation on the same plane as the leading partial dislocation in (a) to form perfect dislocation. (c) If the trailing partial dislocation nucleates from the immediate adjacent similar plane to the leading partial dislocation then the twin embryo is formed. (d) If the trailing partial dislocation is on a different plane to the leading partial dislocation then two SFs are formed. FCC atoms are removed to show partial dislocations, twin, and SFs after CNA. White-colored atoms are immediately surrounding the crack and red-colored atoms are HCP atoms as per CNA. Reproduced with permission from reference [178]. (e) Crack-tip activity in HCP Zr. Nucleation of dislocation from the crack tip. Enlarged visualization of propagating dislocation is shown inside figure (e). The atoms are colored after CNA as red for HCP atoms and blue for atoms other than HCP. Reproduced with permission from reference [187]. (f) Crack-tip activity in BCC Fe. Nucleation of twin from the crack tip. The arrows indicate the orientations of parent crystal and twin. The atoms are colored after CNA as blue for BCC atoms and white for atoms other than BCC. Reproduced with permission from reference [139]. (For interpretation of the references to color in this figure legend, the reader is referred to the web version of this article.)

of partials or faults were observed with increased stress. Between void size 10 and 100 nm, the stress required to nucleate dislocation decreases as void size increases. Above 100 nm, multiple nucleation of dislocation occur with rapid void growth [184].

In the process of nucleation of a twin from the crack tip, the initial step is the nucleation of the leading partial dislocation from the crack tip leaving behind a SF (Fig. 17a). If the trailing partial dislocation is on the same plane as the leading partial dislocation, they combine to form perfect dislocation [185] (Fig. 17b). If the trailing partial dislocation is on the adjacent plane to the leading partial dislocation, then this creates a twin embryo [178] (Fig. 17c). Formation of twins from the crack tip can inhibit further crack growth [186] thus increasing the critical stress for crack propagation. A similar process of nucleation of twins is observed in single crystal configurations (Section 3.1). If the trailing partial dislocation is on a different plane than the leading partial dislocation, then it creates two SFs as in Fig. 17d. A similar observation is seen in the Σ 11 GB configuration emitting SFs in Fig. 12a. Nucleation of dislocation from the crack tip in HCP Zr follows a similar process as above as seen in Fig. 17e [187]. The twinned region from the crack tip in BCC Fe at an advanced stage is shown in Fig. 17f [139]. The advanced stage of deformation twinning involves nucleation of consecutive partial dislocations from the crack tip which helps the twin embryo to grow along its width and length directions. The selection of the nucleation plane of trailing partial dislocation depends on the crack tip and orientation.

Apart from the nanoscale deformation mechanism formulated as above, there is a conventional energy release rate formulation during crack propagation used in MD simulations [26,35,97,160,188]. The change in the potential energy of the system is attributed to the energy release rate. A similar formulation is applicable for a crack emitting dislocation. Rice introduced the concept of *J*-integral for nucleation of dislocation from crack tip [189]. The energy required for nucleation of dislocation (J_{nucl}) from crack tip in FCC metals is given by

$$J_{nucl} = \frac{8\gamma_{USF}}{(1+cos\theta)sin^2\theta} \tag{17}$$

where γ_{USF} is the unstable SFE and θ is the angle between the nucleating dislocation plane and crack plane. In general, for all metals, Rice gave the criteria for predicting the competition between dislocation nucleation from the crack tip and surface cleavage due to crack [189,190]. The energy required for the onset of crack propagation is the energy required for surface cleavage, $J_c = 2\gamma_s$ where γ_s is the surface energy per unit area of the plane. If $J_c < J_{nucl}$, surface cleavage is energetically favourable and vice versa. In the process of surface cleavage, the crack propagates along close packed planes [191]. Rice proposed a critical stress intensity factor for dislocation emission from crack tip under mode I, K_{Ie} as

$$K_{Ie} = \frac{\sqrt{2G\gamma_{USF}/(1-\nu)}}{\sin\frac{\theta}{2}cos^2\frac{\theta}{2}} \tag{18}$$

The loss of hyperbolicity criterion can also be used to track the crack propagation direction where the strain-softening of the material is observed at the point of tangent modulus losing its positive slope [192]. Talebi et al. [38] used the loss of hyperbolicity criterion in PERMIX, an open-source software framework which can

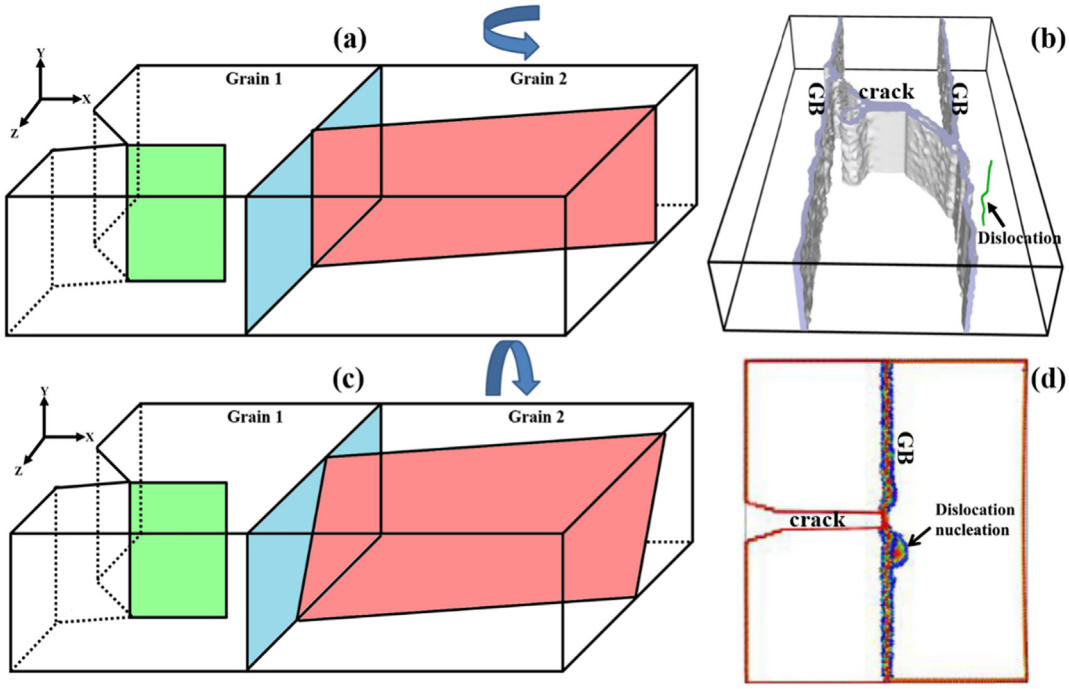

Fig. 18. Schematic illustration of crack propagation through (a) tilt and (c) twist GBs in GB-crack configurations. The interaction of crack with tilt GB in BCC Fe (b), and twist GB in FCC Al (d), shows dislocation nucleation from GB. In (a, c) the green-colored region is the crack propagation plane in grain 1, the blue-colored region is the GB plane and the red-colored region is the possible crack propagation plane in grain 2 and (a) tilt or (c) twist of the plane in grain 2 with respect to the same plane in the grain 1. In (a) the tilt of grain 2 is about Y-axis and in (c) the twist of grain 2 is about X-axis. In (b) the GB and crack surface are grey-colored and nucleating dislocation from GB is green-colored. The atoms are made invisible to visualize the dislocation after DXA. Reproduced with permission from reference [139]. In (d) the atoms are colored as per their centrosymmetry parameter value and the pristine FCC atoms are made invisible. Reproduced with permission from reference [195]. GB, crack, and dislocation are named in or near their entities. (For interpretation of the references to color in this figure legend, the reader is referred to the web version of this article.)

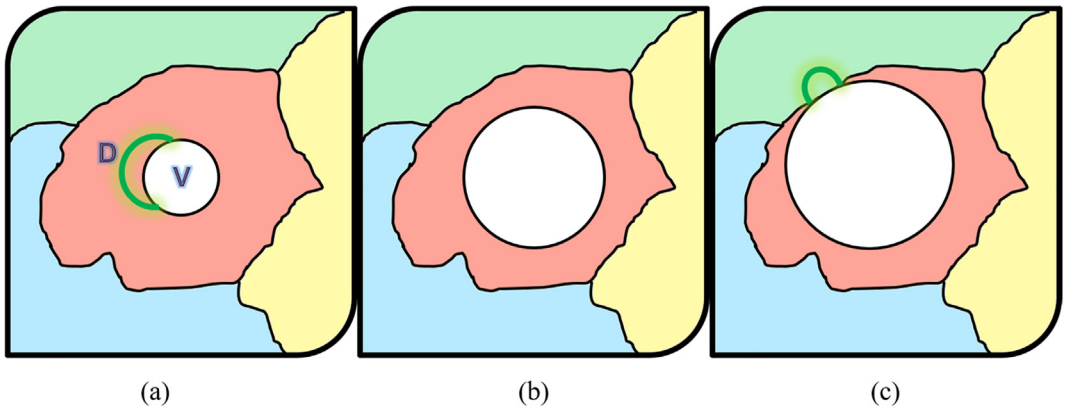

Fig. 19. Schematic illustration of the behavior of a void in the nanocrystalline configuration. (a) The void radius is smaller than the grain size. Dislocation (D) nucleates from the void (V). (b) The void radius is less than but close to the grain size. The region of nucleation of dislocation either from GB or void depends on the GB structure and void radius and is illustrated in Fig. 20. (c) Void size is larger than the grain size or touching the GB. Dislocation nucleates from the interaction region of GB and void. The characters in the image represent D – Dislocation, V – Void.

handle both atomistic and finite elements to study multiscale modeling of fracture. The multiscale model in PERMIX considers an atomistic model near the crack region. Budarapu et al. [37] validated the multiscale model using two-dimension and three-dimension crack growth.

3.4. GB-void/crack Configurations

The complexity of the problem increases while dealing with configurations with more than one type of defect. GB configurations may increase or decrease the strength depending on the type of GB, the direction of loading, and GB spacing (Fig. 11). In GB configurations, the presence of crack decreases the strength and initiates failure sooner than the configurations without crack [139,187,193]. A conclusion based on the strength of the configurations with GB and crack in various metals is difficult as there are several factors such as GB types and crack size and orientation influencing the strength of the material. However, they help in understanding the interaction of crack with GB and resistance of crack propagation or dislocation nucleation from the crack tip. In the case of crack propagation with the nucleation of dislocation from the crack tip, the dislocation interacts with the GB. This interaction could lead to a change in the GB structure resulting in a decrease in the strength and critical stress for dislocation nucle-

ation from the GB. This also helps in the crack growth in the GB vicinity. Crack propagation is faster through GB where its structure is amorphous. The resistance to crack propagation is larger in twist GBs than in tilt GBs [168]. The twist angle of the GB configurations determines whether the crack propagation is through or along the GB plane [194]. Schematic illustration of crack propagation through tilt and twist GBs is shown in Fig. 18a and 18c [168]. The green-colored region is the crack propagation plane in grain 1, the blue-colored region is the GB plane and the red-colored region is the possible crack propagation plane in grain 2. In Fig. 18a tilt of grain 2 is about Y-axis and in Fig. 18c twist of grain 2 is about X-axis. Dislocation or crack propagation from grain 1 to 2 through GB depends on the orientation of the crack plane (red-colored region) in grain 2. When the tilt or twist angle is less than 15°, dislocation migration from its LAGB plane is observed irrespective of the tilt and twist GB configurations [139,168]. For the misorientation angle greater than 15°, the crack growth rate in tilt GB configuration is higher than that of the twist GB configuration [168]. The initial interaction of crack and GB dissociates the GB structure aiding dislocation nucleation from GB. In tilt GB configuration, the possibility of nucleating a perfect dislocation is higher than in twist GB configurations as seen in Fig. 18b and d respectively. In tilt GB configuration, the nucleation site of dislocation is at the interaction of crack and GB [139], while in twist GB configuration, the nucleation of partial dislocation is 1.2 nm away from the interaction site of crack and GB as seen by Chandra et al. [195]. The extent of dissociation of the GB structure is more in twist than in tilt grain boundaries. So, the crack propagates in the GB region (twist configuration) and the crack plane is changed which decreases the crack growth rate. In case of dislocation propagation through the GB plane, tilt GB configurations allow dislocation propagation in the next grain without altering its type while in twist GB configurations dislocation composes of sessile and glissile types [194]. Sessile dislocation also contributes to the hindrance of crack growth.

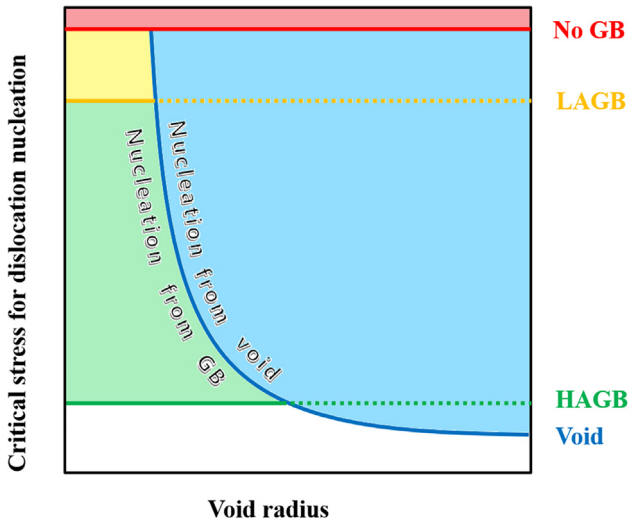

Fig. 20. Schematic illustration of regions with the possibilities of dislocation nucleation in GB-crack configuration. Straight lines represent a border between distinct GB types classified based on the critical stress for dislocation nucleation from GB and a blue-colored curve represents that of the void. The blue-colored curve also represents the critical radius of the void R_c. The regions are colored depending on the requirement of critical stress for dislocation nucleation. The red-colored region represents configuration with no GB, possibly single crystal with voids of all sizes can nucleate dislocation. The yellow-colored region represents dislocation nucleation from LAGBs. The green-colored region represents dislocation nucleation from HAGBs but non-Σ GBs. The white-colored region represents other GBs that have less critical stress for dislocation nucleation. The blue-colored region represents dislocation nucleation from the void. The dotted lines show that GB has no effect in this region. (For interpretation of the references to color in this figure legend, the reader is referred to the web version of this article.)

Dislocation nucleation from a void in single crystal configuration is already detailed in Section 3.3 using Figs. 15 and 16. In configurations with both GB and void, there is a competition between GB and void for nucleation of dislocation. Jing et al. proposed a criterion based on critical stress for the growth of a void in nanocrystalline configuration [151]. In nanocrystalline configurations with small voids within a larger grain, the initial deformation is similar to that of a void in single crystal configuration as schematically shown in Fig. 19a. The void emits a dislocation which interacts with the GB. Depending on the type of the GB, dislocation propagates on the slip plane of the adjacent grain. The void growth rate is minimum in this type of configuration. In configurations with larger voids touching the GBs, dislocations are emitted at the region where the void and GB meet as schematically shown in Fig. 19c. The void growth rate is higher in this type of configuration. Void size also affects the maximum stress achieved during uniaxial deformation. Shang et al. [196] showed that a small void (radius less than 0.5 nm) at the GB plane had higher maximum stress than that of the GB configuration without void during the tensile simulation. This phenomenon was also reported by Tang et al. [159] in single crystal configuration with a void radius of less than 0.5 nm. In case if the void size is smaller than the grain size and doesn't touch the GB (Fig. 19b), then there exists a critical void size radius R_c in grain of size d, at which the behaviour transforms from dislocation emission from GB to dislocation emission from void. For void sizes below R_c, emission of dislocation will be from GB. The critical stress required for dislocation emission, σ from the void of radius R in nanocrystalline configuration is given by the equation [151]:

$$\sigma = \frac{\left[A^2+\delta^2\right]^2}{2\delta A}\left[\tau_c + \frac{Gb^2}{\pi R(1-\nu)}\frac{A(A^4+0.25)}{(A^2+0.5)^2(A^4-0.25)}\right] \tag{19}$$

$$A = \frac{\rho b + R\sqrt{1-\delta^2}}{R} \tag{20}$$

where G is the shear modulus, ν is the Poisson's ratio, b is the magnitude of Burger vector of the emitted dislocation, τ_c is the critical resolved shear stress, δ is a parameter dependent on the distance from the void to the emitted dislocation, and ρ is a material-dependent parameter and can take values of 1, 1.5, or 2.

$R = R_c$ when the critical stress required for dislocation emission from void equals the critical stress required for dislocation emission from GB. The critical stress required for dislocation emission from GB is constant for a particular GB type. For $R > R_c$, the dislocation emission from the void becomes energetically favorable. The schematic illustration of regions with the possibilities of dislocation nucleation in GB-void configuration is shown in Fig. 20 [151]. Fig. 20 is a plot between critical stress required for dislocation nucleation for different GB configurations and void radius. The horizontal straight lines represent the critical stress for dislocation nucleation from GB. The blue-colored curve demarcates the regime where dislocations nucleate from GB and that where dislocations nucleate from voids (equation (19)). The red-colored region represents configuration with no GB (GB energy is zero), possibly a single crystal with voids of all sizes can nucleate dislocation. However, void radius less than 0.5 nm requires high stress for dislocation nucleation almost equal to the shear stress in a pristine configuration. Assuming the critical stress required for dislocation nucleation from GB is directly proportional to the maximum stress during uniaxial simulation, LAGBs and Σ 3 GBs exhibiting low GB energy have high critical stress for dislocation nucleation. In configurations with low GB energy, most of the void sizes nucleate dis-

locations as R_c shifts to the left in the plot in Fig. 20. The green-colored region represents non-CSL HAGBs. Dislocations nucleate from dissociated structures of the GB region. As HAGBs have a higher dissociated structure than that of Σ GBs, they tend to have lower critical stress required for dislocation nucleation and multiple dislocation nucleation sites exist along the GB plane. The white-colored region in Fig. 20 represents other GBs that have less critical stress for dislocation nucleation and have not been quantified yet. The blue-colored region represents dislocation nucleation from the void. The above explanation is from the perspective of the various GBs. From the perspective of various void sizes, there exists a critical void radius which is the intersection of the void curve and GB line in Fig. 20. Below the critical radius, dislocation nucleation from GB is favored.

4. Summary and conclusion

This article has detailed the deformation behavior of various configurations based on the defects (dislocation, void, crack, GB) carried out using MD technique in the past few decades. This article has summarized results from simulation having ⟨100⟩ for FCC and BCC, and ⟨0001⟩ for HCP as the loading direction for single crystals and void/crack configurations. There are studies with other crystallographic directions as loading directions which have not been covered in this article [6,35]. The dimensions of the simulation box also influence the dislocation nucleation and strength [133,197,198], however, this has not been discussed in this article. The maximum stress values during atomistic uniaxial simulations were tabulated and plotted to show the effect of temperature and strain rate on single crystal, GB/interface, and void/crack. The available data from the literature (Tables 1-3, Figs. 6, 11, and 14) match well with the data shown in Fig. 2 of the maximum stress values following the order: single crystal configurations > GB/interface configurations > crack configurations. One set of simulations with various defect configurations with common temperature and strain rate is shown in Fig. 5 to visualize stress–strain response. Deformation of single crystal configurations is characterized by nucleation of dislocations from the surface [89,135,199–203] while that of GB configurations showed nucleation from dissociated structures (low symmetry structure and less number of neighbors around atoms in the GB region) in the GBs [142] and the crack configurations showed nucleation from crack tip [176]. Nucleating dislocations can be partial or perfect depending on the surface roughness in single crystal configuration [135], GB type in GB configuration, and crack tip orientation and sharpness in the crack configuration. Deformation twins form as a result of the movement of partial dislocations [159]. Single crystal with a crack increases the complexity of the interaction of dislocation with the free surface. The cross-over of complexity happens in the nanocrystalline configurations with voids or cracks. However, the initial deformation mechanism can be predicted by identifying the entity (GB or void) emitting the first dislocation.

Some of the advancements and outputs from MD simulations are listed:

1. Deformation of metals involves slip on the preferred slip system based on Schmid's law. There is also the normal stress to the glide plane (non-Schmid factor) which affects dislocation nucleation.
2. Strain rate determines the axial location of failure in nanowires during tensile loading.
3. SFE contributes to the nucleation of dislocation or twin in single crystal configurations, GB configurations, and void/crack configurations. The competition between nucleation of partial and perfect dislocations and twins in single crystal configuration is influenced by a geometric factor (critical width of the simulation box) and SFE along with temperature and loading conditions. The material with low SFE has a high possibility of twinning. In crack configurations, crack tip and orientation also influence the nucleation of partial and perfect dislocation and twin. *J*-integral and critical stress intensity factor in crack configurations are also functions of SFE.
4. The formation of twin is observed after the trailing partial dislocation nucleate on a similar adjacent plane to the leading partial dislocation. Phase transformation is observed after the movement of partial dislocation in the twinning region. These observations are similar for single crystal and crack configurations.
5. The dislocation nucleates from the dissociated structures of the GB. The dislocation nucleation happens at lower stress and strain values for HAGBs as compared to LAGBs and Σ GBs.
6. The strength of nanocrystalline configurations is inversely proportional to the nanograin size. Its strength depends not only on grain size but also on SFE and dislocation splitting distance, which determines whether the deformation mechanism is dislocation nucleation or GB sliding.
7. In configurations with GB and crack, the resistance to crack propagation is larger in twist GBs than tilt GBs.
8. In configurations with GB and void, the GB structure, its energy, and the void radius play important roles in deciding whether the dislocation nucleates at the GB or on the void surface. Low GB energy configurations such as LAGBs and Σ GBs make the void surface energetically favorable for dislocation nucleation. LAGBs and Σ 3 GB require high critical stress to nucleate dislocations during the uniaxial simulation.

The fundamental insights obtained from the classical molecular dynamics simulation studies provided a reasonable understanding of the intricate details of deformation micromechanisms in various materials which are not readily available from the state-of-the-art experimental techniques. Moreover, the information gained from the atomistic simulation studies can also be utilized in developing new materials with improved properties by incorporating grain boundaries which exhibit superior crack resistance.

Declaration of Competing Interest

The authors declare that they have no known competing financial interests or personal relationships that could have appeared to influence the work reported in this paper.

Acknowledgement

This work was supported under the BARC 12th plan project number XII-N-R&D-25 "Experimental Studies for Ageing and Life Extension of Nuclear Components".

References

[1] Cherkaoui M, Capolungo L. Atomistic and continuum modeling of nanocrystalline materials deformation mechanisms and scale. Transition 2009. https://doi.org/10.1017/CBO9781107415324.004.
[2] Frenkel D, Smit B. Understanding molecular simulation: From algorithms to applications. Academic Press; 1996.
[3] Meyer M, Pontikis V. Computer simulation in materials science interatomic potentials, simulation techniques and applications. Springer; 1991. doi:10.1007/978-94-011-3546-7.
[4] Binder K, Heermann DW. Monte Carlo simulation in statistical physics an introduction, 5th ed.; 2010. doi:10.1017/CBO9781107415324.004.
[5] Ashurst WT, Hoover WG. Microscopic fracture studies in the two-dimensional triangular lattice. Phys Rev B 1976;14:1465–73. https://doi.org/10.1103/PhysRevB.14.1465.

[6] Lao J, Naghdi Tam M, Pinisetty D, Gupta N. Molecular dynamics simulation of FCC metallic nanowires: a review. Jom 2013;65:175–84. https://doi.org/10.1007/s11837-012-0465-3.
[7] Pommier S, Gravouil A, Combescure A, Moës N. Extended finite element method for crack propagation; 2011. doi:10.1002/9781118622650.
[8] Buehler MJ. Atomistic modeling of materials failure. Springer; 2008.
[9] Kröger M, Stankovic I, Hess S. Towards multiscale modeling of metals via embedded particle computer simulation. Multiscale Model Simul 2003;1:25–39. https://doi.org/10.1137/s1540345902408470.
[10] Rountree CL, Kalia RK, Lidorikis E, Nakano A, Van Brutzel L, Vashishta P. Atomistic aspects of crack propagation in brittle materials: Multimillion atom molecular dynamics simulations. Annu Rev Mater Sci 2002;32:377–400. https://doi.org/10.1146/annurev.matsci.32.111201.142017.
[11] De Koning M, Kurtz RJ, Bulatov VV, Henager CH, Hoagland RG, Cai W, et al. Modeling of dislocation-grain boundary interactions in FCC metals. J Nucl Mater 2003;323:281–9. https://doi.org/10.1016/j.jnucmat.2003.08.008.
[12] Mehrez H, Ciraci S. Yielding and fracture mechanisms of nanowires. Phys Rev B - Condens Matter Mater Phys 1997;56:12632–42. https://doi.org/10.1103/PhysRevB.56.12632.
[13] Raabe D. Comput Mater Sci 1998. https://doi.org/10.1016/j.commatsci.2010.11.011.
[14] Provatas N, Elder K. Phase-Field Methods in Materials Science and Engineering. KGaA: WILEY-VCH Verlag GmbH & Co; 2010.
[15] Gilbert HD. Miniaturization. New York: Reinhold; n.d.
[16] Liu L, Wang J, Gong SK, Mao SX. Atomistic observation of a crack tip approaching coherent twin boundaries. Sci Rep 2014;4:3–6. https://doi.org/10.1038/srep04397.
[17] Marian J, Cai W, Bulatov VV. Dynamic transitions from smooth to rough to twinning in dislocation motion. Nat Mater 2004;3:158–63. https://doi.org/10.1038/nmat1072.
[18] Bulatov VV, Cai W. Computer simulations of dislocations; 2006. doi:10.1080/0889311x.2015.1084507.
[19] Liu X, Sun L, Zhu L, Liu J, Lu K, Lu J. High-order hierarchical nanotwins with superior strength and ductility. Acta Mater 2018;149:397–406. https://doi.org/10.1016/j.actamat.2018.01.047.
[20] Sun B, Ouyang W, Ren J, Mi L, Guo W. Fcc→bcc→hcp successive phase transformations in the strained ultrathin copper film: a molecular dynamic simulation study. Mater Chem Phys 2019;223:171–82. https://doi.org/10.1016/j.matchemphys.2018.09.045.
[21] Kedharnath A, Kapoor R, Sarkar A. Atomistic simulation of interaction of collision cascade with different types of grain boundaries in α-Fe. J Nucl Mater 2019;523:444–57. https://doi.org/10.1016/j.jnucmat.2019.06.021.
[22] Parrinello M, Rahman A. Polymorphic transitions in single crystals: A new molecular dynamics method. J Appl Phys 1981;52:7182–90. https://doi.org/10.1063/1.328693.
[23] Singh CV, Mateos AJ, Warner DH. Atomistic simulations of dislocation-precipitate interactions emphasize importance of cross-slip. Scr Mater 2011;64:398–401. https://doi.org/10.1016/j.scriptamat.2010.10.041.
[24] Tschopp MA, Spearot DE, McDowell DL. Atomistic simulations of homogeneous dislocation nucleation in single crystal copper. Model Simul Mater Sci Eng 2007;15:693–709. https://doi.org/10.1088/0965-0393/15/7/001.
[25] Guo ZX. Multiscale materials modelling Fundamentals and applications. Cambridge: Woodhead Publishing and Maney Publishing; 2007.
[26] Buehler MJ, Abraham FF, Gao H. Hyperelasticity governs dynamic fracture at a critical length scale. Nature 2003;426:141–6. https://doi.org/10.1038/nature02096.
[27] Singh D, Parashar A, Kedharnath A, Kapoor R, Sarkar A. Effect of symmetrical and asymmetrical tilt grain boundaries on the tensile deformation of zirconium bicrystals: a MD-based study. J Mater Sci 2019;54:3082–95. https://doi.org/10.1007/s10853-018-3032-7.
[28] Kedharnath A, Sarkar A, Kapoor R, Balaji S, David C, Dutta D, et al. Irradiation studies on a reactor pressure vessel steel using Fe+ ion. Mater Res Express 2019;6. https://doi.org/10.1088/2053-1591/ab3f8b.
[29] Verdhan N, Kapoor R. Interaction of dislocations with low angle tilt boundaries in fcc crystals. Comput Mater Sci 2015;98:149–57. https://doi.org/10.1016/j.commatsci.2014.11.006.
[30] Kapoor R, Verdhan N. Interaction of dislocation pile-up with a low-angle tilt boundary: a discrete dislocation dynamics study. Philos Mag 2017;97:465–88. https://doi.org/10.1080/14786435.2016.1266102.
[31] Verdhan N, Kapoor R. Comparison of the strength of binary dislocation junctions in fcc crystals. Indian J Mater Sci 2014;2014:1–5. https://doi.org/10.1155/2014/715356.
[32] Kwon YW, Bang H. The finite element method using MATLAB; 2000. doi:10.1201/9781315275949.
[33] Tadmor EB, Miller RE. Modeling materials: Continuum, atomistic and multiscale techniques; 2011. doi:10.1017/CBO9781139003582.
[34] Rappaz M, Bellet M, Deville M. Numerical modeling in materials science and engineering; 2003. doi:10.1016/s1369-7021(03)00336-5.
[35] Zhang J, Ghosh S. Molecular dynamics based study and characterization of deformation mechanisms near a crack in a crystalline material. J Mech Phys Solids 2013;61:1670–90. https://doi.org/10.1016/j.jmps.2013.04.004.
[36] Lyu D, Li S. Multiscale crystal defect dynamics: a coarse-grained lattice defect model based on crystal microstructure. J Mech Phys Solids 2017;107:379–410. https://doi.org/10.1016/j.jmps.2017.07.006.
[37] Budarapu PR, Gracie R, Yang SW, Zhuang X, Rabczuk T. Efficient coarse graining in multiscale modeling of fracture. Theor Appl Fract Mech 2014;69:126–43. https://doi.org/10.1016/j.tafmec.2013.12.004.
[38] Talebi H, Silani M, Bordas SPA, Kerfriden P, Rabczuk T. A computational library for multiscale modeling of material failure. Comput Mech 2014;53:1047–71. https://doi.org/10.1007/s00466-013-0948-2.
[39] Plimpton S. Fast parallel algorithms for short-range molecular dynamics. J Comput Phys 1995;117:1–19. https://doi.org/10.1006/jcph.1995.1039.
[40] Berendsen HJC, van der Spoel D, van Drunen R. GROMACS: a message-passing parallel molecular dynamics implementation. Comput Phys Commun 1995;91:43–56. https://doi.org/10.1016/0010-4655(95)00042-E.
[41] Phillips JC, Braun R, Wang W, Gumbart J, Tajkhorshid E, Villa E, et al. Scalable molecular dynamics with NAMD. J Comput Chem 2005;26:1781–802. https://doi.org/10.1002/jcc.20289.
[42] Brooks BR, Brooks C, Mackerell AD, Nilsson L, Petrella RJ, Roux B, et al. Molecular dynamics simulation package. J Comput Chem 2009;30:1545–614. https://doi.org/10.1002/jcc.21287.CHARMM.
[43] Green MS. Markoff random processes and the statistical mechanics of time-dependent phenomena. J Chem Phys 1952;20:1281–95. https://doi.org/10.1063/1.1700722.
[44] Helfand E. Transport coefficients from dissipation in a canonical ensemble. Phys Rev 1960;119:1–9.
[45] Hoover WG. Atomistic nonequilibrium computer simulations. Phys A Stat Mech Its Appl 1983;118:111–22. https://doi.org/10.1016/0378-4371(83)90180-2.
[46] Gibson JB, Goland AN, Milgram M, Vineyard GH. Dynamics of radiation damage. Phys Rev 1960;120:1229–53. https://doi.org/10.1103/PhysRev.120.1229.
[47] Holian BL, Hoover WG, Moran B, Straub GK. Shock-wave structure via nonequilibrium molecular dynamics and Navier-Stokes continuum mechanics. Phys Rev A 1980;22:2798–808. https://doi.org/10.1103/PhysRevA.22.2798.
[48] Verlet L. Computer "experiments" on classical fluids. I. Thermodynamical properties of lennard-jones molecules. Phys Rev 1967;159:98–103. https://doi.org/10.1088/0022-3727/9/2/008.
[49] Nose S, Klein ML. Constant pressure molecular dynamics for molecular systems. Mol Phys 1983;50:1055–76.
[50] Nosé S. A unified formulation of the constant temperature molecular dynamics methods. J Chem Phys 1984;81:511–9. https://doi.org/10.1063/1.447334.
[51] Holian BL, Ravelo R. Fracture simulations using large-scale molecular dynamics. Phys Rev B 1995;51:11275–88. https://doi.org/10.1103/PhysRevB.51.11275.
[52] Hoover WG. Nonequilibrium molecular dynamics. Nucl Physics, Sect A 1992;545:523–36. https://doi.org/10.1016/0375-9474(92)90490-B.
[53] Lynden-Bell RM. A simulation study of induced disorder, failure and fracture of perfect metal crystals under uniaxial tension. J Phys Condens Matter 1995;7:4603–24. https://doi.org/10.1088/0953-8984/7/24/003.
[54] Zhu H, Averback RS. Molecular dynamics simulations of densification processes in nanocrystalline materials. Mater Sci Eng A 1995;204:96–100. https://doi.org/10.1016/0921-5093(95)09944-1.
[55] Doyama M. Simulation of plastic deformation of small iron and copper single crystals. Nucl Inst Methods Phys Res B 1995;102:107–12. https://doi.org/10.1016/0168-583X(95)80125-6.
[56] Abraham FF, Broughton JQ. Large-scale simulations of brittle and ductile failure in fcc crystals. Comput Mater Sci 2002;10:1–9. https://doi.org/10.1016/s0927-0256(97)00092-x.
[57] Branício PS, Rino J-P. Large deformation and amorphization of Ni nanowires under uniaxial strain: a molecular dynamics study. Phys Rev B 2000;62:16950–5. https://doi.org/10.1103/PhysRevB.62.16950.
[58] Peng P, Liao G, Shi T, Tang Z, Gao Y. Molecular dynamic simulations of nanoindentation in aluminum thin film on silicon substrate. Appl Surf Sci 2010;256:6284–90. https://doi.org/10.1016/j.apsusc.2010.04.005.
[59] Mahata A, Sikdar K. Molecular dynamics simulation of nanometer scale mechanical properties of hexagonal MgLi alloy. J Magnes Alloy 2016;4:36–43. https://doi.org/10.1016/j.jma.2015.12.001.
[60] Macmillan NH, Kelly A. Some limitations in the use of Morse potentials for calculating ideal strengths of metals. Mater Sci Eng 1973;12:79–86. https://doi.org/10.1016/0025-5416(73)90130-4.
[61] Setoodeh AR, Attariani H, Khosrownejad M. Nickel nanowires under uniaxial loads: a molecular dynamics simulation study. Comput Mater Sci 2008;44:378–84. https://doi.org/10.1016/j.commatsci.2008.03.035.
[62] Finnis MW, Sinclair JE. A simple empirical N-body potential for transition metals. Philos Mag A Phys Condens Matter, Struct Defects Mech Prop 1984;50:45–55. https://doi.org/10.1080/01418618408244210.
[63] Daw MS, Baskes MI. Embedded-atom method: derivation and application to impurities, surfaces, and other defects in metals. Phys Rev B 1984;29:6443–53. https://doi.org/10.1103/PhysRevB.29.6443.
[64] Rawat S, Mitra N. Evolution of tension twinning in single crystal Ti under compressive uniaxial strain conditions. Comput Mater Sci 2018;141:302–12. https://doi.org/10.1016/j.commatsci.2017.09.041.
[65] Rawat S, Mitra N. Compression twinning and structural phase transformation of single crystal titanium under uniaxial compressive strain conditions: comparison of inter-atomic potentials. Comput Mater Sci 2017;126:228–37. https://doi.org/10.1016/j.commatsci.2016.09.034.

[66] Rawat S, Mitra N. Molecular dynamics investigation of c-axis deformation of single crystal Ti under uniaxial stress conditions: Evolution of compression twinning and dislocations. Comput Mater Sci 2018;141:19–29. https://doi.org/10.1016/j.commatsci.2017.09.015.
[67] Thompson AP, Plimpton SJ, Mattson W. General formulation of pressure and stress tensor for arbitrary many-body interaction potentials under periodic boundary conditions. J Chem Phys 2009;131:1–6. https://doi.org/10.1063/1.3245303.
[68] Wang CJ, Wang CJ, Xu J, Zhang P, Shan DB, Guo B, Wang ZL. Tensile deformation behaviors of pure nickel fine wire with a few grains across diameter. Trans Nonferrous Met Soc China (English Ed) 2016;26:1765–74. https://doi.org/10.1016/S1003-6326(16)64287-5.
[69] Gurao NP, Kapoor R, Suwas S. Effect of strain rate on evolution of the deformation microstructure and texture in polycrystalline copper and nickel. Metall Mater Trans A Phys Metall Mater Sci 2010;41:2794–804. https://doi.org/10.1007/s11661-010-0360-x.
[70] Suzuki T, Vinogradov A, Hashimoto S. Strength enhancement and deformation behavior of gold after equal-channel angular pressing. Mater Trans 2004;45:2200–8. https://doi.org/10.2320/matertrans.45.2200.
[71] Hou Y, Mi X, Xie H, Zhang W, Huang G, Peng L, et al. Size effect on mechanical properties and deformation behavior of pure copper wires considering free surface grains. Materials (Basel) 2020;13:1–11. https://doi.org/10.3390/ma13204563.
[72] Kundu A, Kapoor R, Tewari R, Chakravartty JK. Severe plastic deformation of copper using multiple compression in a channel die. Scr Mater 2008;58:235–8. https://doi.org/10.1016/j.scriptamat.2007.09.046.
[73] Abd El Aal MI, Sadawy MM. Influence of ECAP as grain refinement technique on microstructure evolution, mechanical properties and corrosion behavior of pure aluminum. Trans Nonferrous Met Soc China (English Ed) 2015;25:3865–76. https://doi.org/10.1016/S1003-6326(15)64034-1.
[74] Wei Q, Jiao T, Mathaudhu SN, Ma E, Hartwig KT, Ramesh KT. Microstructure and mechanical properties of tantalum after equal channel angular extrusion (ECAE). Mater Sci Eng A 2003;358:266–72. https://doi.org/10.1016/S0921-5093(03)00305-8.
[75] Rabkin E, Nam HS, Srolovitz DJ. Atomistic simulation of the deformation of gold nanopillars. Acta Mater 2007;55:2085–99. https://doi.org/10.1016/j.actamat.2006.10.058.
[76] Yamakov V, Wolf D, Phillpot SR, Mukherjee AK, Gleiter H. Deformation-mechanism map for nanocrystalline metals by molecular-dynamics simulation. Nat Mater 2004;3:43–7. https://doi.org/10.1038/nmat1035.
[77] Heyes DM. Pressure tensor of partial-charge and point-dipole lattices with bulk and surface geometries. Phys Rev B 1994;49:755–64. https://doi.org/10.1103/PhysRevB.49.755.
[78] Thompson AP, Plimpton SJ, Mattson W. General formulation of pressure and stress tensor for arbitrary many-body interaction potentials under periodic boundary conditions. J Chem Phys 2009;131. https://doi.org/10.1063/1.3245303.
[79] Koh SJA, Lee HP, Lu C, Cheng QH. Molecular dynamics simulation of a solid platinum nanowire under uniaxial tensile strain: Temperature and strain-rate effects. Phys Rev B - Condens Matter Mater Phys 2005;72:1–11. https://doi.org/10.1103/PhysRevB.72.085414.
[80] Komanduri R, Chandrasekaran N, Raff LM. Molecular Dynamics (MD) simulation of uniaxial tension of some single-crystal cubic metals at nanolevel. Int J Mech Sci 2001;43:2237–60. https://doi.org/10.1016/S0020-7403(01)00043-1.
[81] Koh SJA, Lee HP. Molecular dynamics simulation of size and strain rate dependent mechanical response of FCC metallic nanowires. Nanotechnology 2006;17:3451–67. https://doi.org/10.1088/0957-4484/17/14/018.
[82] Wang D, Zhao J, Hu S, Yin X, Liang S, Liu Y, et al. Where, and how, does a nanowire break?. Nano Lett 2007;7:1208–12. https://doi.org/10.1021/nl0629512.
[83] Zhang L, Lu C, Tieu K, Pei L, Zhao X, Cheng K. Molecular dynamics study on the grain boundary dislocation source in nanocrystalline copper under tensile loading. Mater Res Express 2015;2. https://doi.org/10.1088/2053-1591/2/3/035009.
[84] Stukowski A, Albe K. Extracting dislocations and non-dislocation crystal defects from atomistic simulation data. Model Simul Mater Sci Eng 2010;18. https://doi.org/10.1088/0965-0393/18/8/085001.
[85] Stukowski A. Visualization and analysis of atomistic simulation data with OVITO-the Open Visualization Tool. Model Simul Mater Sci Eng 2010;18:. https://doi.org/10.1088/0965-0393/18/1/015012015012.
[86] Li J. AtomEye: an efficient atomistic configuration viewer. Model Simul Mater Sci Eng 2003;11:173–7. https://doi.org/10.1088/0965-0393/11/2/305.
[87] Wang JP, Yue ZF, Wen ZX, Zhang DX, Liu CY. Orientation effects on the tensile properties of single crystal nickel with nanovoid: Atomistic simulation. Comput Mater Sci 2017;132:116–24. https://doi.org/10.1016/j.commatsci.2017.02.024.
[88] Liu H, Zhou J. Plasticity in nanotwinned polycrystalline Ni nanowires under uniaxial compression. Mater Lett 2016;163:179–82. https://doi.org/10.1016/j.matlet.2015.10.068.
[89] Wen YH, Zhu ZZ, Zhu RZ. Molecular dynamics study of the mechanical behavior of nickel nanowire: strain rate effects. Comput Mater Sci 2008;41:553–60. https://doi.org/10.1016/j.commatsci.2007.05.012.
[90] Chen DL, Chen TC. Mechanical properties of Au nanowires under uniaxial tension with high strain-rate by molecular dynamics. Nanotechnology 2005;16:2972–81. https://doi.org/10.1088/0957-4484/16/12/041.
[91] Tang DM, Ren CL, Wang MS, Wei X, Kawamoto N, Liu C, et al. Mechanical properties of Si nanowires as revealed by in situ transmission electron microscopy and molecular dynamics simulations. Nano Lett 2012;12:1898–904. https://doi.org/10.1021/nl204282v.
[92] Liang T, Zhou D, Wu Z, Shi P, Chen X. Length-dependent dual-mechanism-controlled failure modes in silver penta-twinned nanowires. Nanoscale 2018;10:20565–77. https://doi.org/10.1039/c8nr03507e.
[93] Rohith P, Sainath G, Choudhary BK. Molecular dynamics simulation studies on the influence of aspect ratio on tensile deformation and failure behaviour of ⟨1 0 0⟩ copper nanowires. Comput Mater Sci 2017;138:34–41. https://doi.org/10.1016/j.commatsci.2017.06.019.
[94] Joshi SK, Pandey K, Singh SK, Dubey S. Molecular dynamics simulations of deformation behaviour of gold nanowires. J Nanotechnol 2019;2019:1–5. https://doi.org/10.1155/2019/5710749.
[95] Rohith P, Sainath G, Srinivasan VS. Effect of size, temperature and strain rate on dislocation density and deformation mechanisms in Cu nanowires. Phys B Condens Matter 2019;561:136–40. https://doi.org/10.1016/j.physb.2019.03.003.
[96] Sainath G, Choudhary BK. Atomistic simulations on ductile-brittle transition in 111 BCC Fe nanowires. J Appl Phys 2017;122. https://doi.org/10.1063/1.4999090.
[97] Liu T, Groh S. Atomistic modeling of the crack-void interaction in α-Fe. Mater Sci Eng A 2014;609:255–65. https://doi.org/10.1016/j.msea.2014.05.005.
[98] Ma B, Rao Q, He Y. Molecular dynamics simulation of temperature effect on tensile mechanical properties of single crystal tungsten nanowire. Comput Mater Sci 2016;117:40–4. https://doi.org/10.1016/j.commatsci.2016.01.001.
[99] Xu S, Guo YF, Ngan AHW. A molecular dynamics study on the orientation, size, and dislocation confinement effects on the plastic deformation of Al nanopillars. Int J Plast 2013;43:116–27. https://doi.org/10.1016/j.ijplas.2012.11.002.
[100] Wang WD, Yi CL, Fan KQ. Molecular dynamics study on temperature and strain rate dependences of mechanical tensile properties of ultrathin nickel nanowires. Trans Nonferrous Met Soc China (English Ed) 2013;23:3353–61. https://doi.org/10.1016/S1003-6326(13)62875-7.
[101] Amigo N, Gutiérrez G, Ignat M. Atomistic simulation of single crystal copper nanowires under tensile stress: influence of silver impurities in the emission of dislocations. Comput Mater Sci 2014;87:76–82. https://doi.org/10.1016/j.commatsci.2014.02.014.
[102] Ren J, Sun Q, Xiao L, Ding X, Sun J. Phase transformation behavior in titanium single-crystal nanopillars under [0 0 0 1] orientation tension: a molecular dynamics simulation. Comput Mater Sci 2014;92:8–12. https://doi.org/10.1016/j.commatsci.2014.05.018.
[103] Aghababaei R, Joshi SP. Micromechanics of tensile twinning in magnesium gleaned from molecular dynamics simulations. Acta Mater 2014;69:326–42. https://doi.org/10.1016/j.actamat.2014.01.014.
[104] Healy CJ, Ackland GJ. Molecular dynamics simulations of compression-tension asymmetry in plasticity of Fe nanopillars. Acta Mater 2014;70:105–12. https://doi.org/10.1016/j.actamat.2014.02.021.
[105] Saha S, Mojumder S, Mahboob M, Islam MZ. Effect of temperature and geometric parameters on elastic properties of tungsten nanowire: A molecular dynamics study. AIP Conf Proc 2016;1754. https://doi.org/10.1063/1.4958353.
[106] An M, Deng Q, Li Y, Song H, Su M, Cai J. Molecular dynamics study of tension-compression asymmetry of nanocrystal α-Ti with stacking fault. Mater Des 2017;127:204–14. https://doi.org/10.1016/j.matdes.2017.04.076.
[107] Chang L, Zhou CY, Wen LL, Li J, He XH. Molecular dynamics study of strain rate effects on tensile behavior of single crystal titanium nanowire. Comput Mater Sci 2017;128:348–58. https://doi.org/10.1016/j.commatsci.2016.11.034.
[108] Chang L, Zhou CY, Liu HX, Li J, He XH. Orientation and strain rate dependent tensile behavior of single crystal titanium nanowires by molecular dynamics simulations. J Mater Sci Technol 2018;34:864–77. https://doi.org/10.1016/j.jmst.2017.03.011.
[109] Sutton AP, Chen J. Long-range finnis-sinclair potentials. Philos Mag Lett 1990;61:139–46. https://doi.org/10.1080/09500839008206493.
[110] Chantasiriwan S, Milstein F. Embedded-atom models of 12 cubic metals incorporating second- and third-order elastic-moduli data. Phys Rev B - Condens Matter Mater Phys 1998;58:5996–6005. https://doi.org/10.1103/PhysRevB.58.5996.
[111] Morse PM. Diatomic molecules according to the wave mechanics. II. Vibrational levels. Phys Rev 1929;34:57–64.
[112] Johnson RA. Analytic nearest-neighbor model for fcc metals. Phys Rev B 1988;37:3924–31. https://doi.org/10.1103/PhysRevB.37.3924.
[113] Foiles SM, Baskes MI, Daw MS. Embedded-atom-method functions for the fcc metals Cu, Ag, Au, Ni, Pd, Pt, and their alloys. Phys Rev B 1986;33:7983–91. https://doi.org/10.1103/PhysRevB.33.7983.
[114] Cai J, Ye Y. Simple analytical embedded-atom-potential model including a long-range force for fcc metals and their alloys. Phys Rev B - Condens Matter Mater Phys 1996;54:8398–410. https://doi.org/10.1103/PhysRevB.54.8398.
[115] Grochola G, Russo SP, Snook IK. On fitting a gold embedded atom method potential using the force matching method. J Chem Phys 2005;123. https://doi.org/10.1063/1.2124667.
[116] Oh DJ, Johnson RA. Simple embedded atom method model for fcc and hcp metals. Mater Res Soc 1988;3:471–8.
[117] Voter AF, Chen SP. Accurate interatomic potentials for Ni, Al and Ni3Al. MRS Proc 1986;82:175–80. https://doi.org/10.1557/proc-82-175.

[118] Williams PL, Mishin Y, Hamilton JC. An embedded-atom potential for the Cu-Ag system. Model Simul Mater Sci Eng 2006;14:817–33. https://doi.org/10.1088/0965-0393/14/5/002.
[119] Zope RR, Mishin Y. Interatomic potentials for atomistic simulations of the Ti-Al system. Phys Rev B - Condens Matter Mater Phys 2003;68:32–4. https://doi.org/10.1103/PhysRevB.68.024102.
[120] Kim YM, Lee BJ, Baskes MI. Modified embedded-atom method interatomic potentials for Ti and Zr. Phys Rev B - Condens Matter Mater Phys 2006;74. https://doi.org/10.1103/PhysRevB.74.014101.
[121] Ackland GJ. Theoretical study of titanium surfaces and defects with a new many-body potential. Philos Mag A Phys Condens Matter, Struct Defects Mech Prop 1992;66:917–32. https://doi.org/10.1080/01418619208247999.
[122] Sun DY, Mendelev MI, Becker CA, Kudin K, Haxhimali T, Asta M, et al. Crystal-melt interfacial free energies in hcp metals: A molecular dynamics study of Mg. Phys Rev B - Condens Matter Mater Phys 2006;73:1–12. https://doi.org/10.1103/PhysRevB.73.024116.
[123] Mendelev MI, Han S, Srolovitz DJ, Ackland GJ, Sun DY, Asta M. Development of new interatomic potentials appropriate for crystalline and liquid iron. Philos Mag 2003;83:3977–94. https://doi.org/10.1080/14786430310001613264.
[124] Zhou XW, Johnson RA, Wadley HNG. Misfit-energy-increasing dislocations in vapor-deposited CoFe/NiFe multilayers. Phys Rev B - Condens Matter Mater Phys 2004;69:1–10. https://doi.org/10.1103/PhysRevB.69.144113.
[125] Kim YM, Jung IH, Lee BJ. Atomistic modeling of pure Li and Mg-Li system. Model Simul Mater Sci Eng 2012;20. https://doi.org/10.1088/0965-0393/20/3/035005.
[126] Zhou XW, Wadley HNG, Johnson RA, Larson DJ, Tabat N, Cerezo A, et al. Atomic scale structure of sputtered metal multilayers. Acta Mater 2001;49:4005–15. https://doi.org/10.1016/S1359-6454(01)00287-7.
[127] Lin YC, Pen DJ, Chen JN. Molecular dynamic simulation of stress evolution analysis in Cu nanowire under ultra-high strain-rate simple tension. Mol Phys 2014;112:1115–22. https://doi.org/10.1080/00268976.2013.833657.
[128] Li L, Shao JL, Duan SQ, Liang JQ. Atomistic simulation of the fcc-hcp transition in single-crystal Al under uniaxial loading. New J Phys 2010;12. https://doi.org/10.1088/1367-2630/12/3/033011.
[129] Ren J, Sun Q, Xiao L, Sun J. Atomistic simulation of tension-compression asymmetry and its mechanism in titanium single-crystal nanopillars oriented along the [1 1 $\bar{2}$ 0] direction. Comput Mater Sci 2018;147:272–81. https://doi.org/10.1016/j.commatsci.2018.02.029.
[130] Wang BT, Shao JL, Zhang GC, Li WD, Zhang P. Molecular dynamics simulations of hcp/fcc nucleation and growth in bcc iron driven by uniaxial compression. J Phys Condens Matter 2009;21. https://doi.org/10.1088/0953-8984/21/49/495702.
[131] Shao JL, Duan SQ, He AM, Qin CS, Wang P. Dynamic properties of structural transition in iron under uniaxial compression. J Phys Condens Matter 2009;21. https://doi.org/10.1088/0953-8984/21/24/245703.
[132] Wang BT, Shao JL, Zhang GC, Li WD, Zhang P. Nucleation of hcp and fcc phases in bcc iron under uniform compression: classical molecular dynamics simulations. J Phys Condens Matter 2010;22:. https://doi.org/10.1088/0953-8984/22/43/435404435404.
[133] Ren J, Sun Q, Xiao L, Ding X, Sun J. Size-dependent of compression yield strength and deformation mechanism in titanium single-crystal nanopillars orientated 0001 and 1120. Mater Sci Eng A 2014;615:22–8. https://doi.org/10.1016/j.msea.2014.07.065.
[134] Tadmor EB, Bernstein N. A first-principles measure for the twinnability of FCC metals. J Mech Phys Solids 2004;52:2507–19. https://doi.org/10.1016/j.jmps.2004.05.002.
[135] Weinberger CR, Cai W. Plasticity of metal nanowires. J Mater Chem 2012;22:3277–92. https://doi.org/10.1039/c2jm13682a.
[136] Lu Z, Noordhoek MJ, Chernatynskiy A, Sinnott SB, Phillpot SR. Deformation processes in polycrystalline Zr by molecular dynamics simulations. J Nucl Mater 2015;462:147–59. https://doi.org/10.1016/j.jnucmat.2015.03.048.
[137] Rohith P, Sainath G, Choudhary BK. Effect of orientation and mode of loading on deformation behaviour of Cu nanowires. Comput Condens Matter 2018;17. https://doi.org/10.1016/j.cocom.2018.e00330.
[138] Singh D, Parashar A. Effect of symmetric and asymmetric tilt grain boundaries on the tensile behaviour of bcc-Niobium. Comput Mater Sci 2018;143:126–32. https://doi.org/10.1016/j.commatsci.2017.11.005.
[139] Kedharnath A, Panwar AS, Kapoor R. Molecular dynamics simulation of the interaction of a nano-scale crack with grain boundaries in α-Fe. Comput Mater Sci 2017;137:85–99. https://doi.org/10.1016/j.commatsci.2017.05.026.
[140] Chen SD, Zhou YK, Soh AK. Molecular dynamics simulations of mechanical properties for Cu(0 0 1)/Ni(0 0 1) twist boundaries. Comput Mater Sci 2012;61:239–42. https://doi.org/10.1016/j.commatsci.2012.04.035.
[141] Afanasyev KA, Sansoz F. Strengthening in gold nanopillars with nanoscale twins. Nano Lett 2007;7:2056–62. https://doi.org/10.1021/nl070959l.
[142] Spearot DE, Jacob KI, McDowell DL. Dislocation nucleation from bicrystal interfaces with dissociated structure. Int J Plast 2007;23:143–60. https://doi.org/10.1016/j.ijplas.2006.03.008.
[143] Farkas D, Van Petegem S, Derlet PM, Van Swygenhoven H. Dislocation activity and nano-void formation near crack tips in nanocrystalline Ni. Acta Mater 2005;53:3115–23. https://doi.org/10.1016/j.actamat.2005.02.012.
[144] Cao AJ, Wei YG. Molecular dynamics simulation of plastic deformation of nanotwinned copper. J Appl Phys 2007;102:1–6. https://doi.org/10.1063/1.2794884.
[145] Li X, Hu W, Xiao S, Huang WQ. Molecular dynamics simulation of polycrystalline molybdenum nanowires under uniaxial tensile strain: Size effects. Phys E Low-Dimensional Syst Nanostruct 2008;40:3030–6. https://doi.org/10.1016/j.physe.2008.03.013.
[146] Dongare AM, Rajendran AM, Lamattina B, Brenner DW, Zikry MA. Atomic-scale study of plastic-yield criterion in nanocrystalline Cu at high strain rates. Metall Mater Trans A Phys Metall Mater Sci 2010;41:523–31. https://doi.org/10.1007/s11661-009-0113-x.
[147] Gottstein G, Shvindlerman LS. Grain boundary migration in metals: thermodynamics, kinetics, applications, 2nd ed. CRC Press; 2010. doi:10.1061/(asce)0733-9399(2000)126:8(888).
[148] Borovikov V, Mendelev MI, King AH. Effects of solutes on dislocation nucleation from grain boundaries. Int J Plast 2017;90:146–55. https://doi.org/10.1016/j.ijplas.2016.12.009.
[149] Zhao X, Lu C, Tieu AK, Zhan L, Pei L, Huang M. Deformation mechanisms and slip-twin interactions in nanotwinned body-centered cubic iron by molecular dynamics simulations. Comput Mater Sci 2018;147:34–48. https://doi.org/10.1016/j.commatsci.2018.01.054.
[150] Mishin Y, Farkas D, Mehl MJ, Papaconstantopoulos DA. Interatomic potentials for monoatomic metals from experimental data and ab initio calculations. Phys Rev B - Condens Matter Mater Phys 1999;59:3393–407. https://doi.org/10.1103/PhysRevB.59.3393.
[151] Jing P, Yuan L, Shivpuri R, Xu C, Zhang Y, Shan D, et al. Evolution of spherical nanovoids within copper polycrystals during plastic straining: Atomistic investigation. Int J Plast 2018;100:122–41. https://doi.org/10.1016/j.ijplas.2017.09.016.
[152] Jeon JB, Lee BJ, Chang YW. Molecular dynamics simulation study of the effect of grain size on the deformation behavior of nanocrystalline body-centered cubic iron. Scr Mater 2011;64:494–7. https://doi.org/10.1016/j.scriptamat.2010.11.019.
[153] Dongare AM, Rajendran AM, Lamattina B, Zikry MA, Brenner DW. Atomic scale simulations of ductile failure micromechanisms in nanocrystalline Cu at high strain rates. Phys Rev B - Condens Matter Mater Phys 2009;80:1–11. https://doi.org/10.1103/PhysRevB.80.104108.
[154] Spearot DE, Sangid MD. Insights on slip transmission at grain boundaries from atomistic simulations. Curr Opin Solid State Mater Sci 2014;18:188–95. https://doi.org/10.1016/j.cossms.2014.04.001.
[155] Duesbery MS, Vitek V. Plastic anisotropy in b.c.c. transition metals. Acta Metall 1998;46:1481–92.
[156] Duesbery MS, Vitek V, Bowen DK. The effect of shear stress on the screw dislocation core structure in body-centred cubic lattices. Proc R Soc London A Math Phys Sci 1973;332:85–111. https://doi.org/10.1098/rspa.1973.0014.
[157] Zhou K, Liu B, Shao S, Yao Y. Molecular dynamics simulations of tension–compression asymmetry in nanocrystalline copper. Phys Lett Sect A Gen At Solid State Phys 2017;381:1163–8. https://doi.org/10.1016/j.physleta.2017.01.027.
[158] Xu Z, Zhang L, Wang L, Zuo J, Yang M. Computational characterization of the structural and mechanical properties of nanoporous titania. RSC Adv 2019;9:15298–306. https://doi.org/10.1039/c9ra02298h.
[159] Tang Y, Bringa EM, Meyers MA. Ductile tensile failure in metals through initiation and growth of nanosized voids. Acta Mater 2012;60:4856–65. https://doi.org/10.1016/j.actamat.2012.05.030.
[160] Cui CB, Beom HG. Molecular dynamics simulations of edge cracks in copper and aluminum single crystals. Mater Sci Eng A 2014;609:102–9. https://doi.org/10.1016/j.msea.2014.04.101.
[161] Wu WP, Yao ZZ. Molecular dynamics simulation of stress distribution and microstructure evolution ahead of a growing crack in single crystal nickel. Theor Appl Fract Mech 2012;62:67–75. https://doi.org/10.1016/j.tafmec.2013.01.008.
[162] Li YL, Wu WP, Li NL, Qi Y. Cohesive zone representation of crack and void growth in single crystal nickel via molecular dynamics simulation. Comput Mater Sci 2015;104:212–8. https://doi.org/10.1016/j.commatsci.2015.04.011.
[163] Potirniche GP, Horstemeyer MF, Wagner GJ, Gullett PM. A molecular dynamics study of void growth and coalescence in single crystal nickel. Int J Plast 2006;22:257–78. https://doi.org/10.1016/j.ijplas.2005.02.001.
[164] Traiviratana S, Bringa EM, Benson DJ, Meyers MA. Void growth in metals: Atomistic calculations. Acta Mater 2008;56:3874–86. https://doi.org/10.1016/j.actamat.2008.03.047.
[165] Pei L, Lu C, Tieu K, Zhao X, Zhang L, Cheng K, et al. Brittle versus ductile fracture behaviour in nanotwinned FCC crystals. Mater Lett 2015;152:65–7. https://doi.org/10.1016/j.matlet.2015.03.074.
[166] Pei L, Lu C, Zhao X, Zhang L, Cheng K, Michal G, et al. Brittle versus ductile behaviour of nanotwinned copper: a molecular dynamics study. Acta Mater 2015;89:1–13. https://doi.org/10.1016/j.actamat.2015.01.054.
[167] Chandra S, Kumar NN, Samal MK, Chavan VM, Patel RJ. Molecular dynamics simulations of crack growth behavior in Al in the presence of vacancies. Comput Mater Sci 2016;117:518–26. https://doi.org/10.1016/j.commatsci.2016.02.032.
[168] Fang W, Xie H, Yin F, Li J, Khan DF, Fang Q. Molecular dynamics simulation of grain boundary geometry on crack propagation of bi-crystal aluminum. Mater Sci Eng A 2016;666:314–9. https://doi.org/10.1016/j.msea.2016.04.077.
[169] Mishin Y, Mehl MJ, Papaconstantopoulos DA, Voter AF, Kress JD. Structural stability and lattice defects in copper: Ab initio, tight-binding, and

embedded-atom calculations. Phys Rev B - Condens Matter Mater Phys 2001;63:2241061–22410616. https://doi.org/10.1103/PhysRevB.63.224106.
[170] Angelo JE, Moody NR, Baskes MI. Trapping of hydrogen to lattice defects in nickel. Model Simul Mater Sci Eng 1995;3:289–307. https://doi.org/10.1088/0965-0393/3/3/001.
[171] Mendelev MI, Kramer MJ, Becker CA, Asta M. Analysis of semi-empirical interatomic potentials appropriate for simulation of crystalline and liquid Al and Cu. Philos Mag 2008;88:1723–50. https://doi.org/10.1080/14786430802206482.
[172] Gonzáles GLG, González JAO, Paiva VEL, Freire JLF. Crack-tip plastic zone size and shape via DIC. In: Conf. Proc. Soc. Exp. Mech. Ser., 2019: pp. 5–10. doi:10.1007/978-3-319-95879-8_2.
[173] Wu Z, Curtin WA. Brittle and ductile crack-tip behavior in magnesium. Acta Mater 2015;88:1–12. https://doi.org/10.1016/j.actamat.2015.01.023.
[174] Wang L, Liu Q, Shen S. Effects of void-crack interaction and void distribution on crack propagation in single crystal silicon. Eng Fract Mech 2015;146:56–66. https://doi.org/10.1016/j.engfracmech.2015.07.021.
[175] Borodin VA, Vladimirov PV. Molecular dynamics simulations of quasi-brittle crack development in iron. J Nucl Mater 2011;415:320–8. https://doi.org/10.1016/j.jnucmat.2011.04.052.
[176] Borodin VA, Vladimirov PV. Three-dimensional atomistic modeling of microcrack propagation in iron. J Nucl Mater 2011;416:49–54. https://doi.org/10.1016/j.jnucmat.2010.12.224.
[177] Singh D, Sharma P, Jindal S, Kumar P, Kumar P, Parashar A. Atomistic simulations to study crack tip behaviour in single crystal of bcc niobium and hcp zirconium. Curr Appl Phys 2019;19:37–43. https://doi.org/10.1016/j.cap.2018.11.002.
[178] Andric P, Curtin WA. New theory for crack-tip twinning in fcc metals. J Mech Phys Solids 2018;113:144–61. https://doi.org/10.1016/j.jmps.2018.01.016.
[179] Zhao Z, Chu F. Atomic behaviors of crack propagation in bcc iron under dynamic loading rate with rectangular fluctuation. Mater Sci Eng A 2017;707:81–91. https://doi.org/10.1016/j.msea.2017.08.087.
[180] Seppälä ET, Belak J, Rudd RE. Effect of stress triaxiality on void growth in dynamic fracture of metals: a molecular dynamics study. Phys Rev B - Condens Matter Mater Phys 2004;69. https://doi.org/10.1103/PhysRevB.69.134101.
[181] Rice JR, Thomson R. Ductile versus brittle behaviour of crystals. Philos Mag 1974;29:73–97. https://doi.org/10.1080/14786437408213555.
[182] Anderson PM, Rice JR. The stress field and energy of a three-dimensional dislocation loop at a crack tip. J Mech Phys Solids 1987;35:743–69. https://doi.org/10.1016/0022-5096(87)90053-6.
[183] Ruestes CJ, Bringa EM, Stukowski A, Rodríguez Nieva JF, Tang Y, Meyers MA. Plastic deformation of a porous bcc metal containing nanometer sized voids. Comput Mater Sci 2014;88:92–102. https://doi.org/10.1016/j.commatsci.2014.02.047.
[184] Chang HJ, Segurado J, Rodríguez De La Fuente O, Pabón BM, Llorca J. Molecular dynamics modeling and simulation of void growth in two dimensions. Model Simul Mater Sci Eng 2013;21. https://doi.org/10.1088/0965-0393/21/7/075010.
[185] Borodin VA, Vladimirov PV, Möslang A. The effects of temperature on (0 0 1) ⟨1 1 0⟩ crack propagation in bcc iron. J Nucl Mater 2013;442:S612–7. https://doi.org/10.1016/j.jnucmat.2012.10.035.
[186] Zhao Z, Qin Z, Chu F. Atomistic scale fracture behavior of the bcc iron with 1 1 0 crack under dynamic rectangular loading rate. Comput Mater Sci 2019;158:178–91. https://doi.org/10.1016/j.commatsci.2018.11.020.
[187] Singh D, Parashar A, Kedharnath A, Kapoor R, Sarkar A. Molecular dynamics-based simulations to study crack tip interaction with symmetrical and asymmetrical tilt grain boundaries in Zr. J Nucl Mater 2019;526:. https://doi.org/10.1016/j.jnucmat.2019.151739151739.
[188] Zhou Y, Yang Z, Lu Z. Dynamic crack propagation in copper bicrystals grain boundary by atomistic simulation. Mater Sci Eng A 2014;599:116–24. https://doi.org/10.1016/j.msea.2014.01.070.
[189] Rice JR. Dislocation nucleation from a crack tip: An analysis based on the Peierls concept. J Mech Phys Solids 1992;40:239–71. https://doi.org/10.1016/S0022-5096(05)80012-2.
[190] Zimmerman JA, Jones RE. The application of an atomistic J-integral to a ductile crack. J Phys Condens Matter 2013;25. https://doi.org/10.1088/0953-8984/25/15/155402.
[191] Zhang Y, Jiang S, Zhu X, Zhao Y. Mechanisms of crack propagation in nanoscale single crystal, bicrystal and tricrystal nickels based on molecular dynamics simulation. Results Phys 2017;7:1722–33. https://doi.org/10.1016/j.rinp.2017.04.039.
[192] Belytschko T, Chen H, Xu J, Zi G. Dynamic crack propagation based on loss of hyperbolicity and a new discontinuous enrichment. Int J Numer Methods Eng 2003;58:1873–905. https://doi.org/10.1002/nme.941.
[193] Singh D, Parashar A. Effect of crack on the tensile strength of a bicrystal Zr - A MD based evaluation. Mater Sci Forum 2020;978:487–91. https://doi.org/10.4028/www.scientific.net/MSF.978.487.
[194] Zhang Y, Jiang S, Zhu X, Zhao Y. Influence of twist angle on crack propagation of nanoscale bicrystal nickel film based on molecular dynamics simulation. Phys E Low-Dimensional Syst Nanostructures 2017;87:281–94. https://doi.org/10.1016/j.physe.2016.11.005.
[195] Chandra S, Naveen Kumar N, Samal MK, Chavan VM, Raghunathan S. An atomistic insight into the fracture behavior of bicrystal aluminum containing twist grain boundaries. Comput Mater Sci 2017;130:268–81. https://doi.org/10.1016/j.commatsci.2017.01.023.
[196] Shang J, Yang F, Li C, Wei N, Tan X. Size effect on the plastic deformation of pre-void Ni/Ni3Al interface under uniaxial tension: A molecular dynamics simulation. Comput Mater Sci 2018;148:200–6. https://doi.org/10.1016/j.commatsci.2018.02.046.
[197] Sainath G, Choudhary BK. Molecular dynamics simulations on size dependent tensile deformation behaviour of [110] oriented body centred cubic iron nanowires. Mater Sci Eng A 2015;640:98–105. https://doi.org/10.1016/j.msea.2015.05.084.
[198] Sainath G, Choudhary BK, Jayakumar T. Molecular dynamics simulation studies on the size dependent tensile deformation and fracture behaviour of body centred cubic iron nanowires. Comput Mater Sci 2015;104:76–83. https://doi.org/10.1016/j.commatsci.2015.03.053.
[199] Rohith P, Sainath G, Goyal S, Nagesha A, Srinivasan VS. Role of axial twin boundaries on deformation mechanisms in Cu nanopillars. Philos Mag 2020;100:529–50. https://doi.org/10.1080/14786435.2019.1695163.
[200] Weinberger CR, Jennings AT, Kang K, Greer JR. Atomistic simulations and continuum modeling of dislocation nucleation and strength in gold nanowires. J Mech Phys Solids 2012;60:84–103. https://doi.org/10.1016/j.jmps.2011.09.010.
[201] Sainath G, Choudhary BK. Twinning to slip transition in ultrathin BCC Fe nanowires. Phys Lett Sect A Gen At Solid State Phys 2018;382:1047–51. https://doi.org/10.1016/j.physleta.2018.02.007.
[202] Sainath G, Choudhary BK. Deformation behaviour of body centered cubic Fe nanowires under tensile and compressive loading, ArXiv Prepr. ArXiv1409.3324; 2014.
[203] Sainath G, Rohith P, Choudhary BK. Size dependent deformation behaviour and dislocation mechanisms in ⟨1 0 0⟩ Cu nanowires. Philos Mag 2017;97:2632–57. https://doi.org/10.1080/14786435.2017.1347300.